

# Thesis Title

by

E. Ross



A thesis submitted to the  
University of Birmingham  
for the degree of  
DOCTOR OF PHILOSOPHY

Solar and Stellar Physics Group (SASP)

School of Physics and Astronomy

University of Birmingham

Birmingham, B15 2TT

Month 20XX

# Contents

<b>List of Figures</b>	<b>iv</b>
<b>List of Tables</b>	<b>v</b>
<b>List of Abbreviations</b>	<b>viii</b>
<b>1 Introduction</b>	<b>1</b>
1.1 Solar Activity . . . . .	1
1.1.1 Background . . . . .	1
1.1.2 Features of Solar Activity . . . . .	7
1.2 Space Weather . . . . .	13
1.2.1 Background . . . . .	13
1.2.2 Impacts of Space Weather . . . . .	15
1.3 Cosmic Rays . . . . .	19
1.3.1 Background . . . . .	19
1.3.2 Cosmic Rays in the Atmosphere . . . . .	22
1.3.3 Cosmic Ray Detectors . . . . .	24
1.3.4 Cosmic Ray Observations of Solar Activity and Space Weather	27
1.4 The HiSPARC Experiment . . . . .	34
1.4.1 Background . . . . .	34
1.4.2 HiSPARC Detector and Station Configuration . . . . .	35
1.4.3 HiSPARC Data Acquisition . . . . .	39
1.5 Thesis Structure . . . . .	44
<b>Bibliography</b>	<b>46</b>

# List of Figures

1.1	Schematic diagram of the main processes that drive the changes to the Sun’s magnetic field. Staring from a poloidal field on the left, it is shown how the $\Omega$ -effect generates a toroidal field. On the top we see a demonstration of the creation of small-scale poloidal magnetic fields, the $\alpha$ -effect. On the bottom we see a demonstration of the the Babcock-Leighton mechanism, diffusion and meridional flows. Finally, on the right we see the recovery of a poloidal field with opposite polarity. Adapted from <a href="#">Sanchez et al. (2014)</a> . . . . .	2
1.2	Monthly averaged sunspot number since 1750 ( <a href="#">Hathaway &amp; Upton, 2017</a> ). Black points indicate a full month of data, and then a traffic light system is in place to represent data quality, i.e. green for a near-complete month of data, amber for near 50% duty cycle, and red for a very low data duty cycle. . . . .	4
1.3	Top panel: shows the latitudinal distribution of sunspots over time (also known as a “Butterfly Diagram”) and the colour of the points depict the area of the disc. Bottom panel: shows the average daily area of sunspots on the visible solar disc. Taken from <a href="#">Hathaway &amp; Upton (2017)</a> . . . . .	5
1.4	UK National Risk Register for hazards, diseases, accidents, and societal risks showing space weather as a medium-high risk ( <a href="#">Cabinet Office, 2017</a> ) . . . . .	16
1.5	The sources and effects of space weather. Impacts are shown including loss of telecommunications and GNSS, increased radiation levels, and ground induced currents (ESA/Science Office, <a href="#">CC BY-SA 3.0 IGO</a> ) . . . . .	16
1.6	Cosmic ray differential energy spectrum using data measured by several experiments. The inset shows the H/He ratio at constant rigidity ( <a href="#">Particle Data Group et al., 2020</a> ) . . . . .	21

1.7	Schematic diagrams of two NM configurations: (a) the original Simpson's 12-tube IGY NM is shown where the paraffin reflector is represented by the outer dotted blocks; the lead producer is represented by the cross-hatched section; the paraffin moderator is represented by the inner dotted blocks; finally the gas-filled proportional counters are denoted by the black circles/tubes. (b) the modern NM64 is shown on the right in its 6-tube configuration where the polyethylene reflector is represented by the outer dotted section; the lead producer is represented by the cross-hatched area; within the producer is a cylindrical polyethylene moderator denoted by the dotted ring; finally in the centre of each tube is a gas-filled proportional counter. In each figure the top schematic is a top-down drawing and the bottom is an end-on drawing. Taken from <a href="#">Kang et al. (2012)</a> . . . . .	25
1.8	Schematic design of a typical scintillation muon detector with back-end electronics ( <a href="#">Gloeckler, 2010</a> ) . . . . .	26
1.9	Cosmic ray flux measured at the Climax NM (solid line) and rescaled SSN (dotted line) taken from <a href="#">Hathaway (2015)</a> . The vertical lines denote changes in the Sun's global magnetic field polarity, where: A+ indicates positive polarity at the North Pole; A− indicates negative polarity at the North Pole. . . . .	28
1.10	A two-step Forbush decrease measured at three NM stations, Deep River, Mt. Wellington, Kerguelen, in July 1982 ( <a href="#">Cane, 2000</a> ). The thicker black line indicates the average of the count rates from the three stations. Arrows show the start of the two decreases caused by the shock and the ICME ejecta. . . . .	29
1.11	A schematic diagram of an ICME-driven FD taken from <a href="#">Cane (2000)</a> . It shows the different cosmic ray responses from two paths, indicated by A and B. A experiences the shock and ejecta, therefore experiencing a two-step FD; B only experiences the shock, therefore experiencing a single decrease. The time of shock passage is indicated by a solid, vertical line marked, S; the start and end times of ejecta passage are indicated by vertical, dashed lines marked T1 and T2, respectively. . . . .	30
1.12	A GLE measured at nine NM stations in October 1989, taken from <a href="#">Cramp, J. L. et al. (1997)</a> . . . . .	31
1.13	A schematic diagram of the 'garden hose' field line taken from <a href="#">Duldig et al. (1993)</a> . . . . .	33
1.14	Schematic diagram of the HiSPARC scintillation detector. (A): PMT; (B): light-guide adaptor; (C): light-guide; (D): scintillator. . . . .	36
1.15	Typical formations of two-detector and four-detector stations ( <a href="#">Fokkema, 2012</a> ; <a href="#">van Dam et al., 2020b</a> ). In each, the black circle denotes a GPS antenna which is located in between the detectors to provide a precise timestamp for each signal. . . . .	38
1.16	A schematic diagram showing the configuration and interfaces between the HiSPARC hardware for a two-detector station. . . . .	39

1.17	(a): An example PMT signal after digital conversion by the HiSPARC electronics box. The horizontal lines denote: the noise cut-off (dotted line), which is used for setting a limit when integrating the pulse height, to give the pulse integral; the low-voltage threshold (dash-dot); the high-voltage threshold (dashed). The role of the high- and low-voltage thresholds are described in the text below. (b) The pulse height distribution over the course of a single day from HiSPARC station 501. The vertical lines show the low-voltage threshold (dash-dot) and the high-voltage threshold (dashed). . . . .	40
1.18	Schematic data acquisition of an event ( <a href="#">Fokkema, 2012</a> ). The dashed vertical lines denote the epochs of the pre-trigger, coincidence, and post-trigger windows. The grey, shaded region shows the data reduction window and data outside this window are not stored. The dotted, horizontal lines denote the low- and high-voltage thresholds. .	42

# List of Tables

1.1	Most prominent decay modes of the mesonic components of CR air showers and of muons. Note: $K^-$ modes are charge conjugates of the decay modes below ( <a href="#">Particle Data Group et al., 2020</a> ) . . . . .	23
-----	--	----

# List of Abbreviations

**AR** Active Region.

**AS** Air Shower.

**BiSON** Birmingham Solar Oscillations Network.

**BMR** Bipolar Magnetic Region.

**CIR** Corotating Interaction Region.

**CMA** Central Moving Average.

**CMB** Cosmic Microwave Background.

**CME** Coronal Mass Ejection.

**CR** Cosmic Ray.

**DAQ** Data Acquisition.

**EAS** Extensive Air Shower.

**ER** Ephemeral Region.

**FD** Forbush Decrease.

**FE** Forbush Effect.

**FEID** Forbush Effects and Interplanetary-disturbances Database.

**FPGA** Field Programmable Gate Array.

**GCR** Galactic Cosmic Ray.

**GIC** Ground Induced Current.

**GLE** Ground Level Enhancement.

**GNMN** Global Neutron Monitor Network.

**GNSS** Global Navigation Satellite System.

**GPS** Global Positioning System.

**GZK** Greisen-Zatsepin-Kuzmin.

**HiSPARC** High School Project on Astrophysics and Research with Cosmics.

**HV** High Voltage.

**ICME** Interplanetary Coronal Mass Ejection.

**IMF** Interplanetary Magnetic Field.

**ISSN** International Sun Spot Number.

**LOS** Line Of Sight.

**MD** Muon Detector.

**MIP** Minimum Ionising Particle.

**MOSWOC** Met Office Space Weather Operations Centre.

**MPV** Most Probable Value.

**NM** Neutron Monitor.

**NOAA** National Oceanic and Atmospheric Administration.

**PCR** Primary Cosmic Ray.

**PMMA** Polymethylmethacrylate.

**PMT** Photo Multiplier Tube.

**SAPPHiRE** Simulation and Analysis Program Package for HiSPARC Research and Education.

**SCR** Solar Cosmic Ray.

**SEP** Solar Energetic Particle.

**SILSO** Sunspot Index and Long-term Solar Observations.

**SMMF** Solar Mean Magnetic Field.

**SOHO/LASCO** Solar and Heliospheric Observatory Large Angle and Spectrometric Coronagraph.

**SRB** Solar Radio Burst.

**SSN** Sun Spot Number.



**SWPC** Space Weather Prediction Center.

**UHECR** Ultra-High-Energy Cosmic Ray.

**UMR** Unipolar Magnetic Region.

**WDC** World Data Center.

# 1 Introduction

## 1.1 Solar Activity

### 1.1.1 Background

Solar activity varies periodically, with a duration of approximately 11 years, known as the solar cycle ([Hathaway, 2015](#)). The solar cycle is a magnetic effect and is driven by the Sun's dynamo processes. Magnetic fields and the ionised plasma in the Sun's interior move together, as the magnetic field is 'frozen' to the plasma; thermonuclear reactions and the inductive action of plasma occur in the Sun's core, giving rise to complex structures and dynamics in the outer layers of the Sun ([Charbonneau, 2020](#)).



It is well known that the 11-year solar activity cycle is in fact a 22-year cycle – the Hale cycle – which describes the alternating polarity and the full regeneration of the large-scale solar magnetic field ([Hathaway, 2015](#); [Charbonneau, 2020](#)). The Sun's large-scale magnetic field alternates between a poloidal field and a toroidal field ([Charbonneau, 2020](#)), i.e. following the sequence:

$$P(+) \rightarrow T \rightarrow P(-) \rightarrow T \rightarrow P(+) \rightarrow T \rightarrow \dots, \quad (1.1)$$

where the  $P$  and  $T$  refer to poloidal and toroidal fields, respectively,  $(+)$  and  $(-)$  refer to the signs of the poloidal field polarity, and the different colours denote the  $\sim 11$ -year cycles.

Starting with a poloidal field with positive polarity,  $P(+)$ , differential rotation causes shearing of the magnetic field and it wraps around the Sun, as shown in Figure 1.1. As a result the magnetic field becomes concentrated at certain latitudes above and below the equator. This is named the  $\Omega$ -effect and is responsible for the creation of a toroidal field,  $T$  (Hathaway, 2015; Charbonneau, 2020).

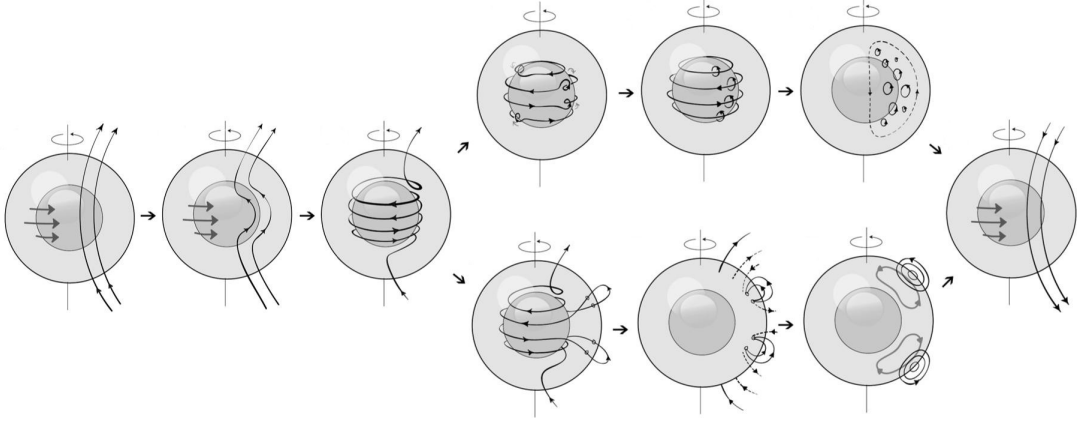


Figure 1.1: Schematic diagram of the main processes that drive the changes to the Sun's magnetic field. Starting from a poloidal field on the left, it is shown how the  $\Omega$ -effect generates a toroidal field. On the top we see a demonstration of the creation of small-scale poloidal magnetic fields, the  $\alpha$ -effect. On the bottom we see a demonstration of the Babcock-Leighton mechanism, diffusion and meridional flows. Finally, on the right we see the recovery of a poloidal field with opposite polarity. Adapted from Sanchez et al. (2014).

The recovery of the poloidal field is not as straightforward. To recover a poloidal with opposite polarity,  $P(-)$ , there are two main schools of thought, as shown in Figure 1.1 (Sanchez et al., 2014). One is based on the role of cyclonic turbulence and can be described by mean-field electrodynamics (Charbonneau, 2020). Due to the influence of the Coriolis force, helical motions lift and twist the magnetic field, known as the  $\alpha$ -effect (Charbonneau, 2020). The degree of twist can produce sources of poloidal field and through the combination of many small, accumulating elements, we get the generation of a new poloidal field with opposite polarity (Charbonneau, 2020). Another mechanism is the Babcock-Leighton model (Babcock, 1961; Leighton, 1964) whereby tilted bipolar regions of magnetic field undergo diffusion and cross-equatorial reconnection. Through the action of diffusion and meridional flows, poloidal flux is advected to the poles which creates a new poloidal

field with opposite polarity (Sheeley, 2005; Charbonneau, 2020). There is debate in the literature about which mechanism dominates the recovery of the poloidal field.

These processes repeat with each cycle from poloidal-to-toroidal field and back to a poloidal field with opposite polarity (i.e.  $P(+) \rightarrow T \rightarrow P(-)$ ), in  $\sim 11$  years. Therefore it takes  $\sim 22$  years for the full magnetic cycle, the Hale cycle, to regenerate a poloidal field with the same polarity (i.e.  $P(+) \rightarrow \dots \rightarrow P(+)$ ).

The earliest observations of solar activity and the solar cycle were of sunspots, which date back to over 2000 years ago (Clark & Stephenson, 1978). Sunspots are dark regions of concentrated, active magnetic flux which cross the photosphere. The earliest observation of solar-cycle variability associated with sunspots was by Schwabe (1844), who found that annual observations of sunspot groups, over a duration 18 years from 1826–1844, showed a cyclic behaviour, with a period of about 10 years.

Following this discovery Wolf (1856, 1859) acquired daily observations of Sun Spot Numbers (SSNs) and extended the records as far back as 1749 (Hathaway, 2015). This used a method of estimating the number of individual sunspots and sunspots groups; these SSNs have since been used to monitor the solar activity cycle (Wolf, 1859, 1861). However, recently, a new, standard time-series of the SSN has been generated to reconcile various discrepancies between different observers (Clette et al., 2016; Clette & Lefvre, 2016). These are the International Sun Spot Number (ISSN) by World Data Center (WDC) Sunspot Index and Long-term Solar Observations (SILSO) of the Royal Observatory of Belgium (SILSO WDC, 2020). These SSNs are shown in Figure 1.2. Each activity cycle has unique characteristics and the SSNs have been used to measure the properties of the cycles, for sunspot observations dating back to the year  $\sim 1750$ .

Observations of sunspots in the 17th Century allowed astronomers to accurately measure the rotation of the Sun’s surface, which they observed to be slightly under four weeks (Casanovas, 1997; Casas et al., 2006; Luminet, 2017). These early obser-



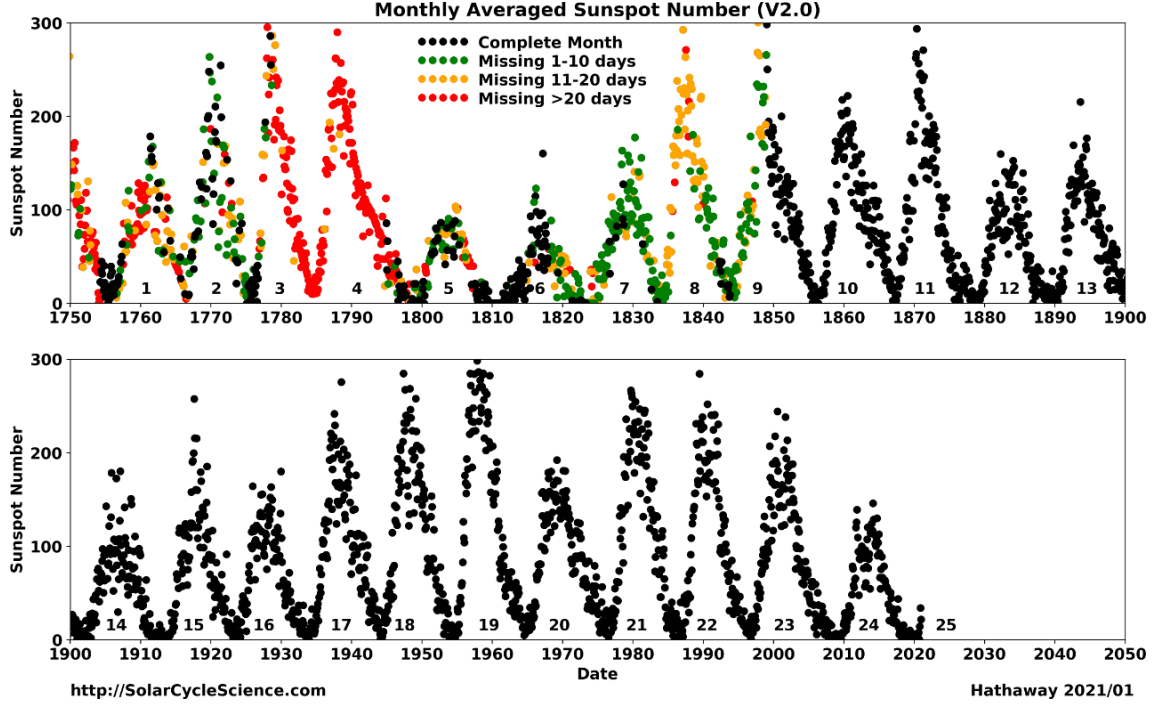


Figure 1.2: Monthly averaged sunspot number since 1750 (Hathaway & Upton, 2017). Black points indicate a full month of data, and then a traffic light system is in place to represent data quality, i.e. green for a near-complete month of data, amber for near 50% duty cycle, and red for a very low data duty cycle.

ations also showed that sunspots did not appear at latitudes higher than  $\sim 29^\circ/30^\circ$  (Casanovas, 1997). Later, it was confirmed that regions of strong surface magnetic activity were not distributed uniformly over the solar surface and also that the Sun exhibited a latitude-dependent differential surface rotation (Lee, 1858).

As the solar cycle evolves the range of latitudes displaying sunspots decreases and the typical latitude of spots slowly drifts towards the equator, with a zone of avoidance near the equator (Hathaway, 2015). This behaviour was first noticed by Carrington (1863) and is known as Spörer’s Law of Zones, illustrated by the “Butterfly Diagram” (Maunder, 1903, 1904), such as the one shown in Figure 1.3.

In the first half of the 20th Century, it was discovered that sunspot groups in both hemispheres were tilted with respect to the Sun’s equator, such that the leading spots (i.e. leading in the sense of the direction of rotation) exist closer to the equator than the following spots. This was first published by Hale et al. (1919) but later defined as Joy’s law. Furthermore, the degree of tilt varies with latitude, with a

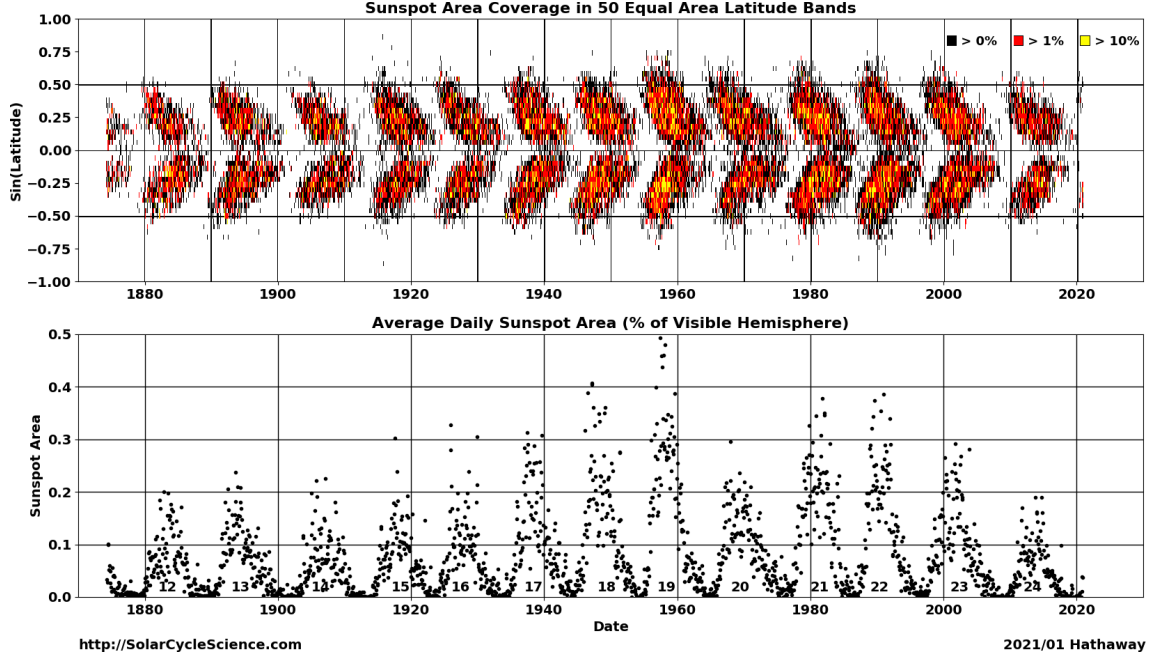


Figure 1.3: Top panel: shows the latitudinal distribution of sunspots over time (also known as a “Butterfly Diagram”) and the colour of the points depict the area of the disc. Bottom panel: shows the average daily area of sunspots on the visible solar disc. Taken from [Hathaway & Upton \(2017\)](#).

larger tilt at higher latitudes, and also with the solar cycle ([Hathaway, 2015](#)). In addition, sunspots groups have opposite polarities in the Northern and Southern hemispheres, and the polarity changes from cycle-to-cycle. This effect is known as Hale’s Polarity Law ([Hale & Nicholson, 1925](#)).

With the invention of the magnetograph ([Babcock, 1953](#)), the Sun’s magnetic field was probed further and it was found that sunspots were a characteristic of a larger phenomenon. It was discovered that sunspots are a small part of larger Active Regions (ARs) of magnetic field, which may be both Bipolar Magnetic Regions (BMRs) or Unipolar Magnetic Regions (UMRs) ([Babcock & Babcock, 1955](#)).

Joy’s law implies that the tilt of BMRs systematically places the leading-polarity-flux at a lower latitude than the following-polarity-flux ([Hathaway, 2015](#)). It is believed that there is a cancellation of leading-polarity flux on the opposite hemisphere near the equator ([Dasi-Espuig et al., 2010](#)).

In very modern literature, the definition of the solar activity cycle has started

to deviate away from counting sunspots and instead tracking the magnetic activity bands over the full, 22-year, Hale cycle (Leamon et al., 2018, 2020). The existence of a “Terminator” has been found, which marks the hand-over from one solar cycle to the next (McIntosh et al., 2014, 2019). The terminator is defined as the abrupt annihilation or cancellation event of the oppositely polarized magnetic activity bands at the solar equator (McIntosh et al., 2019). By employing the Hilbert transform on different proxies of the solar cycle, Leamon et al. (2020) demonstrated a robust method to identify and predict the signature of terminators. The method has since been used to map severe space weather events to a “solar cycle phase clock” (Chapman et al., 2020) and forecast the properties of Solar Cycle 25 (McIntosh et al., 2020). There exists some uncertainty about terminators in the solar physics community; the evidence presented so far suggests this method is robust, but will ultimately be tested with the evolution of Solar Cycle 25.

As discussed, the solar activity cycle exhibits a clear periodicity of approximately 11 years; however, there exist other, short-term periodicities in the solar activity cycle (see Hathaway (2015) for a review). The most prominent other feature in the solar activity cycle is an  $\sim 2$ -year periodicity which manifests as a double peak in the maximum of SSN, known as the Gnevyshev gap (Gnevyshev, 1963, 1967). It was thought that this phenomenon was due to a superposition of sunspots from both hemispheres, slightly out of phase, but it was later confirmed that the Gnevyshev gap occurs in each hemisphere separately (Norton & Gallagher, 2009). The cause of the Gnevyshev effect remains an open question (Hathaway, 2015).

Finally, it has been suggested that long-term variations exist in the solar activity cycle, which consist of grand maxima and grand minima, which have led to the events such as the Maunder minimum (circa 1650–1700) and the Dalton minimum (circa 1790–1820). However, there is little evidence to support this long-term, cyclic variation (Hathaway, 2015).

### 1.1.2 Features of Solar Activity

There are many features that can be observed across the electromagnetic spectrum as a result of solar activity. In addition, with the advent of the magnetograph, solar activity can also be observed with direct measurements of the Sun’s magnetic field, at different spatial scales. Many of these features are used widely in the literature as proxies of the solar activity cycle. Here we discuss these features and their properties.

#### Active Regions

An Active Region (AR) has been defined as all *observable* magnetic phenomena that appear preceding, during, and following the birth of sunspots, including electromagnetic and Solar Energetic Particle (SEP) emission (Kiepenheuer, 1968). However, more generally, they appear when strands of magnetic flux emerge into the visible atmosphere from the solar interior.


van Driel-Gesztelyi & Green (2015) recently proposed a new and more accurate definition of ARs:

*the totality of observable phenomena in a 3D volume represented by the extension of the magnetic field from the photosphere to the corona, revealed by emissions over a wide range of wavelengths accompanying and following the emergence of strong twisted magnetic flux (i.e. kG).*

This definition does not hinge on the appearance of a sunspot, which is important as not all ARs produce spots (van Driel-Gesztelyi & Green, 2015), and clearly defines their conditions and features. ARs comprise of features in the photosphere, chromosphere, and corona; they typically appear as bipolar regions, obeying Hale’s law, Joy’s law, and Spörer’s Law, and display a wide range of sizes and lifetimes. In addition, ARs are typically confined to the specific ‘active’ bands of latitude, between  $\pm 40^\circ$  (Harvey, 2001).

The ARs which produce sunspots are typically 10–100 Mm in size and have lifetimes on the order of several months (Zwaan, 1981; Schrijver & Harvey, 1994;



Canfield, 2001; van Driel-Gesztelyi & Green, 2015). However, it has been observed that  AR exist with lifetimes in the range of days–months (Schrijver & Zwaan, 2008). It is generally accepted that the lifetimes of ARs depend approximately linearly on their size and strength (Canfield, 2001; Schrijver & Zwaan, 2008). The end of an AR is determined by the dispersal of the magnetic flux by convective motion, differential rotation, meridional flows, and magnetic reconnection (Canfield, 2001).

There are several other features that arise out of ARs, such as: faculae, plagues, and networks. Faculae are bright spots visible in the photosphere that appear bright at the limb but are nearly invisible at disc centre. They arise due to small magnetic flux tubes creating pores in the photosphere (Solovev et al., 2019). If the flux tubes are small enough, they are heated by horizontal radiation transfer and the walls appear brighter than the surrounding area, which is known as the ‘hot-wall’ model (Spruit, 1976; Keller et al., 2004). Plages are bright regions in the solar chromosphere and are the chromospheric counterparts of faculae (Pillet et al., 1997). Networks are a product of the decaying remnants of ARs, the merging and cancelling of mixed polarity fields in and around ARs, and ephemeral regions – often referred to as the ‘salt and pepper’ field (Martin, 1988).

## Ephemeral Regions

A short-lived class of Active Regions (ARs) exists, known as Ephemeral Regions (ERs) due to their short lifetimes. ERs have sizes typically less than 20 Mm, lifetimes of a few hours, and produce no sunspots (Harvey, 2001).

ERs emerge rapidly and it is possible that thousands of ERs emerge over the entire solar surface within a 24-hour period (Harvey, 2001). There has been some disagreement in the literature on the temporal evolution of ERs with contradictory statements regarding whether the occurrence of ERs follows the activity cycle (see Harvey & Zwaan, 1993; Hagenaar, 2001; Vieira & Solanki, 2010). However, some studies show compelling evidence that ERs are correlated with the solar activity cycle (see e.g. Vieira & Solanki, 2010; Chaplin et al., 2019, and references therein).

It was also shown that ERs follow the solar activity cycle but with a slight shift in phase compared to the sunspot minimum (Harvey & Martin, 1973; Martin & Harvey, 1979).

Unlike ARs, ERs are spatially located all over the solar disc (Harvey, 2001). Furthermore ERs at high latitudes have been interpreted to be the first emergence of bipolar regions associated with the onset of a new solar cycle. Despite these differences, it has been reported that it is difficult to differentiate between large ERs and small ARs (Harvey, 2001).

## Sunspots

As discussed above, sunspots have been used for centuries as a proxy for solar activity. Sunspots are dark regions on the disc of concentrated magnetic field. The convective heat flow is disrupted due to the magnetic field, therefore leaving the spots cooler than the surrounding photosphere (Solanki, 2003; Hathaway, 2015). Sunspots can sometimes appear in isolation; however, sunspots are generally found in groups, obeying Hale’s law, Joy’s law, and Spörer’s Law. Each sunspot is characterised by a dark, central core, called the *umbra*, and a halo, called the *penumbra* (Howard, 2001; Solanki, 2003). Sunspot groups are an important photometric counterpart of Active Regions (ARs) as the locations of extreme solar activity such as flares and Coronal Mass Ejections (CMEs).

The sizes of sunspots can vary substantially from diameters of around 2000 km, for the smallest sunspots, up to 60 Mm or more (Howard, 2001; Solanki, 2003). The lifetimes of sunspots range from minutes to months (Howard, 2001; Solanki, 2003) and Howard (2001) states that more than half of sunspots have lifetimes  $< 2$  days, 90% of sunspots have lifetimes  $< 11$  days, and it is rare for sunspots to have lifetimes of more than a few months. The lifetime increases linearly with maximum size, following the Gnevyshev-Waldmeier rule (Gnevyshev, 1938; Waldmeier, 1955). The largest spots are generally the survivors of large sunspot groups, appearing as a single spot at least in the later stage of their lifetime (Howard, 2001).



The equatorward drift of sunspots is a well-known characteristic of **the evolution of sunspots** during the solar cycle. Sunspots emerge in active latitudes at around  $\sim 25 - 30^\circ$ , and as the cycle progresses the mean latitude of the spots in each hemisphere steadily decreases. The number of sunspots varies with time with more spots observed during solar maximum and fewer observed at solar minimum (see Fig. 1.2). As such, the sunspot number is the most commonly used proxy for solar activity ([Hathaway, 2015](#)) and the International Sun Spot Number (ISSN) is the most widely used data set due to the length of the available record ([Hathaway, 2015](#)).

Sun Spot Numbers (SSNs) are preserved and disseminated by the World Data Center (WDC) Sunspot Index and Long-term Solar Observations (SILSO) of the Royal Observatory of Belgium ([SILSO WDC, 2020](#)) and are provided as the daily SSN, monthly averages, yearly averages, and the box-car smoothed SSN. The standard smoothing is a 13-month Central Moving Average (CMA) and the solar cycle maxima and minima are usually defined in terms of the smoothed SSN ([Hathaway, 2015](#)).

### 10.7 cm Flux

The 10.7 cm solar flux ( $F_{10.7}$ ) is the disc-integrated radio emission from the Sun at a wavelength of 10.7 cm (in a 100 MHz-wide band centred on 2800 MHz) ([Tapping & Charrois, 1994](#); [Tapping, 2013](#)). It is one of the most widely used indices of solar activity, alongside the SSN, and the  $F_{10.7}$  measure of solar activity has advantages over the SSN in that it is completely objective ([Hathaway, 2015](#)).

The  $F_{10.7}$  comprises of Bremsstrahlung emission from the chromosphere and corona as well as over sunspots, where the magnetic fields are sufficiently strong to produce bright, compact sources from thermal, free-free electron gyroresonances ([Tapping & DeTracey, 1990](#); [Tapping, 2013](#)). However, the dominant component of the  $F_{10.7}$  originates in the low corona ([Tapping & DeTracey, 1990](#)).

The first observations were made in 1946 and have been recorded consistently

since 1947 (Covington, 1969; Tapping, 2013). The data can be acquired from the Laboratory for Atmospheric and Space Physics at University of Colorado (LISIRD, 2019).

## Solar Eruptions

Solar flares are energetic, eruptive events which occur in the region of Active Regions (ARs) and complex sunspot groups (Hathaway, 2015). The first reported solar flare was in 1859, the largest known flare to-date, the Carrington event (Carrington, 1859).

Solar flares follow the solar activity cycle, with more flares occurring at solar maximum, which is likely because during these times there are more ARs on the Sun which tend to be flare-producing (Gopalswamy, 2010; Hathaway, 2015). However, there is a general propensity for more flares to occur during the declining phase of a sunspot cycle (Hathaway, 2015).

Coronal Mass Ejections (CMEs) are manifestations of concentrated solar activity and are associated with the significant release of plasma and accompanying magnetic field ejected from the corona. CMEs are often associated with solar flares but can also occur in isolation, in the absence of a flare (Hathaway, 2015).

CMEs were first discovered in the early 1970s via spacecraft observations and have since routinely been observed (Hathaway, 2015). A database of the properties of all CMEs observed since 1996 by the Solar and Heliospheric Observatory Large Angle and Spectrometric Coronagraph (SOHO/LASCO) instrument exists in the SOHO/LASCO catalogue<sup>1</sup> (Yashiro et al., 2004; Gopalswamy et al., 2009).

Similarly to flares, the frequency of CMEs follow the solar activity cycle, with more CMEs occurring at solar maximum (Gopalswamy, 2010) and is therefore correlated with the Sun Spot Number (SSN) (Webb & Howard, 1994). In addition, physical properties of CMEs such as average speed, size, and the location of ejection from the Sun, etc. also vary with the solar activity cycle (Yashiro et al., 2004).

---

<sup>1</sup>[https://cdaw.gsfc.nasa.gov/CME\\_list/](https://cdaw.gsfc.nasa.gov/CME_list/)

## Total Magnetic Flux

Individual elements of the magnetic field contribute to the large-scale field and determine the Sun’s global magnetic dipole moment and the strength of the field in interplanetary space (Lockwood et al., 1999; Solanki et al., 2000). The total, unsigned, magnetic flux is the amount of flux leaving the Sun and entering the heliosphere, i.e. the combination of AR, Ephemeral Region (ER), and open magnetic flux (Lockwood et al., 1999). The strength of the total magnetic flux and its main components has been shown to vary with the solar activity cycle (Solanki et al., 2002; Vieira & Solanki, 2010; Chaplin et al., 2019). Vieira & Solanki (2010) showed that the respective contributions to the total flux during maximum activity are approximately in the ratio 0.1 : 0.8 : 0.1, for ARs, ERs, and open flux, while the ratios during minimum activity are approximately 0.5 : 0.4 : 0.1, for ARs, ERs, and open flux.



## The Solar Mean Magnetic Field

The Solar Mean Magnetic Field (SMMF) is the mean Line Of Sight (LOS), signed magnetic field when observing the Sun-as-a-star (Scherrer et al., 1977a,b; Garca et al., 1999). The SMMF is surprisingly a non-zero measurement of the imbalance of opposite magnetic flux polarities observed on the full, visible disc of the Sun (Svalgaard et al., 1975), and its amplitude is observed to vary with the solar activity cycle.

The literature on SMMF observations spans several decades; however, the origin of the SMMF remains an open question in solar physics. We give a comprehensive review of the morphology of the SMMF in Section ??, since the analysis and interpretation of SMMF data collected by the Birmingham Solar Oscillations Network (BiSON) is presented in detail in that chapter.

## 1.2 Space Weather

### 1.2.1 Background

Space weather is defined as ([Cannon & Royal Academy of Engineering \(Great Britain\), 2013](#)):

*variations in the Sun, solar wind, magnetosphere, ionosphere, and thermosphere, which can influence the performance and reliability of a variety of space-borne and ground-based technological systems and can also endanger human health and safety.*

Space weather phenomena have been observed over hundreds of years, mainly through observations of the aurorae, but its impacts are slowly becoming more tangible in modern civilisation, as we grow reliant on electronics ([Beggan et al., 2018](#)).

There are two main sources of space weather: (i) those that are solar in nature and (ii) those whose origins are external to the solar system but penetrate into the heliosphere. Space weather manifests itself broadly in three ways:

1. Electromagnetic radiation, which is generally linked with an enhancement in the output of the Sun's spectrum.
2. Magnetic fields/plasma, which can cause disturbances in the Interplanetary Magnetic Field (IMF) and solar wind, and the Earth's magnetosphere.
3. Energetic charged particles, which refer to ionising charged particles and ions.

The nature of their arrival and the resulting impact of these space weather phenomena at Earth depends on their type and energy. Space weather is the resultant product from solar storms – magnetic disturbances on the Sun leading to large bursts of energy release and short-term heliospheric effects – and the general chronology of

events was outlined by [Cannon & Royal Academy of Engineering \(Great Britain\) \(2013\)](#):

1. Storms begin with the evolution of one or more complex sunspot groups and Active Regions (ARs) on the solar surface.
2. Within ARs, one or more solar flares occur and the electromagnetic radiation is detected on Earth within approximately 8 minutes.
3. Solar Energetic Particles (SEPs) are released and are measured at Earth, both using satellites and ground-based detectors, within approximately 15 minutes. SEPs continue to arrive over a period of several hours–days.
4. A Coronal Mass Ejection (CME) occurs and propagates outwards, arriving at a distance of 1 AU within  $\sim 15\text{--}72$  hours. The impact on Earth depends on the CME speed, how close it passes to Earth, and the orientation of the magnetic fields, with southward magnetic field generating the most severe geomagnetic storms because of its interference with Earth’s northward magnetic field resulting in reconnection at the magnetopause.

The largest documented space weather event since modern records began occurred in 1859, the solar super storm known as the “Carrington event” ([Carrington, 1859](#)). The available measurements of this event are limited to geomagnetic field perturbations, as well as eye witness accounts of solar brightening and aurorae ([Cannon & Royal Academy of Engineering \(Great Britain\), 2013](#)). However, recently cosmonuclide measurements from ice cores have been used to learn about the properties of the Carrington event ([Riley, 2012](#)).

Since the beginning of the space age there have been no other super storms, however there have been large storms that have affected the infrastructure and caused a significant economic impact. The consensus is that another storm of the Carrington event level is inevitable and could significantly impact society. There

is a view that a Carrington-like event may occur again in a period of 250 years with a confidence of  $\sim 95\%$  and within a period of 50 years with a confidence of  $\sim 50\%$  ([Cannon & Royal Academy of Engineering \(Great Britain\), 2013](#)); however, it is stressed that these figures should be interpreted with care. It was suggested by [Riley \(2012\)](#) that a Carrington-like event may occur with  $\sim 12\%$  probability between 2012–2022 and later in 2012 a large storm occurred, missing Earth, but it strongly interacted with the STEREO-A satellite ([Russell et al., 2013](#)). This near miss highlights that Carrington-level events are a real threat to society and that we need a method of predicting their occurrence, arrival, and impact.

### 1.2.2 Impacts of Space Weather

Space weather is an increasingly tangible threat to modern infrastructure and society, due to the increasing reliance on electronic technology. In 2011 space weather was added to the UK National Risk Assessment for the first time, and the subsequent National Risk Register in 2012 ([BIS, 2015](#)) where it has remained to-date ([Government, 2020](#)). At the time of writing this thesis, space weather risk was rated as a medium severity/high likelihood risk, at the same level as emerging infectious diseases, poor air quality, and heatwaves (see Figure 1.4) ([Cabinet Office, 2017](#)).

An alarming aspect of Figure 1.4 is that the likelihood of space weather events occurring in 5 years from 2017 was rated the same as pandemic influenza. Finishing this Ph.D. during a global pandemic highlights the importance of taking this risk register very seriously. We should learn from the global response to the COVID-19 pandemic and ensure that the world has a resolute plan to deal with the occurrence of a severe space weather event.

There are many ways that technological systems are impacted by space weather, both on or above ground, and Figure 1.5 displays many of the key impacts that we know of ([Beggan et al., 2018](#)).



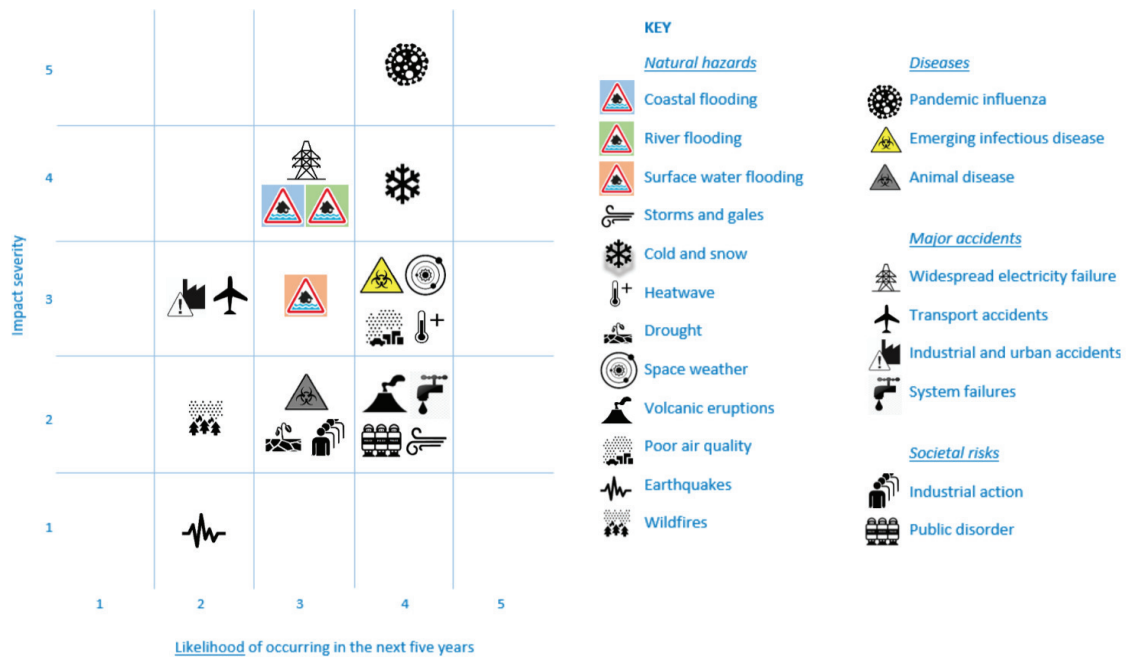


Figure 1.4: UK National Risk Register for hazards, diseases, accidents, and societal risks showing space weather as a medium-high risk (Cabinet Office, 2017)

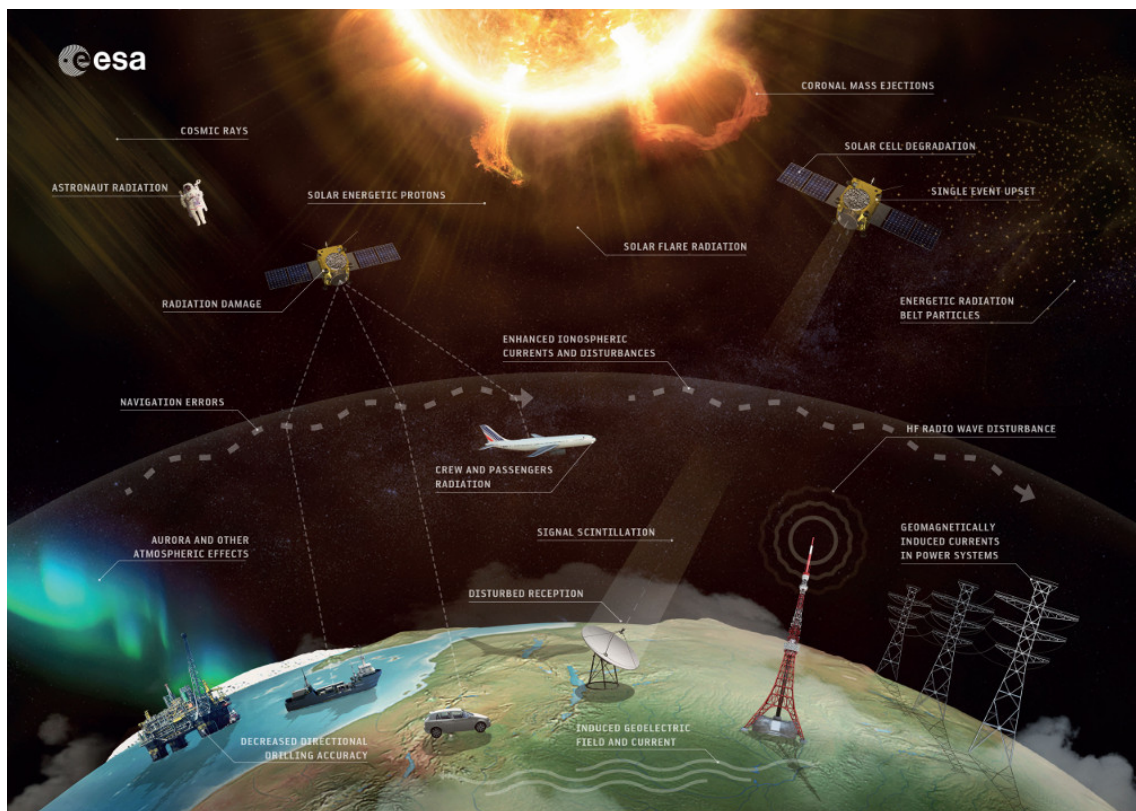


Figure 1.5: The sources and effects of space weather. Impacts are shown including loss of telecommunications and GNSS, increased radiation levels, and ground induced currents (ESA/Science Office, CC BY-SA 3.0 IGO)

As far back as October 1841, it was reported that a solar storm was responsible for railway disruptions around Exeter, due to magnetic disturbances making it impossible to ascertain whether the onward line was clear, leading to delays ([Nature, 1871](#)).

It is possible for space weather events to induce geomagnetic storms that can cause damaging Ground Induced Currents (GICs) within large power grids, causing them to fail. Two such famous cases of GIC grid failures were in Quebec, Canada in 1989 which resulted in the failure of the Quebec-Hydro grid for 9 hours, and the city-wide black-out in Malmö, Sweden, during the Halloween storm in 2003 ([Viljanen, 2011](#); [Beggan et al., 2018](#)).

It was documented that in May 1967, the U.S. Air Force was close to engaging in conflict with its enemies – during those politically tense times – due to the misinterpretation of the effects of space weather ([Knipp et al., 2016](#)). Solar Radio Burst (SRB) induced radio frequency interference was initially interpreted as surveillance jamming, an act of war. Fortunately, the U.S. had begun monitoring the space environment and were able determine that space weather was really the cause of the disruption, hence avoiding further conflict ([Knipp et al., 2016](#)). Furthermore, in more modern times, scintillation effects induced in the ionosphere affect Global Navigation Satellite System (GNSS) communications which has a large societal effect due to our reliance on GNSS ([Cannon & Royal Academy of Engineering \(Great Britain\), 2013](#)) as shown in Figure 1.5.

Solar storms are also responsible for creating sudden increases in ionising radiation which at typical flight altitudes can lead to the risk of malfunctions in aircraft microelectronic systems and unquantified radiation doses to passengers and crew ([Cannon & Royal Academy of Engineering \(Great Britain\), 2013](#)). In orbit, these conditions threaten the operation of satellites and the safety of manned space endeavours which is of particular concern with the current ambitions to return to the Moon and venture to Mars.

There are even concerns that major storms could cause radiation increases at the Earth’s surface, Ground Level Enhancements (GLEs), which may cause malfunctions in microelectronics that are likely to be of increasing concern in the design of safety-critical systems ([Cannon & Royal Academy of Engineering \(Great Britain\), 2013](#)).

Finally, a cost analysis estimated a present-day total U.S. economic cost for a super storm on the scale of the 1859 Carrington event ([Homeier & Wei, 2013](#)). The cost estimated is heavily dependent on the duration of outages, the damages caused, and the availability of spare parts for repair; however they estimated the impact on the U.S. economy to be at around \$0.6–2.6 trillion ([Homeier & Wei, 2013](#)). These figures show the large scale impact that space weather can have on the economy and that mitigation techniques to reduce this cost are of imperative necessity.

Due to the many ways that space weather can impact civilisation, and that it is predicted that there is a significant probability of the re-occurrence of large solar storms, it is easy to understand why space weather forecasting is becoming increasingly more necessary as a mitigation technique.

The U.S. National Oceanic and Atmospheric Administration (NOAA) is the leading global space weather forecasting agency. The NOAA Space Weather Prediction Center (SWPC) gathers data in real-time to describe the conditions of the Sun, heliosphere, magnetosphere, and ionosphere to understand the environment within the heliosphere and on Earth. With these data, the SWPC produces forecasts, warnings, and alerts available to inform anyone concerned and affected by space weather ([NOAA, 2018](#)).

Following the addition of space weather to the UK risk register, the UK Met Office Space Weather Operations Centre (MOSWOC) opened in 2014 ([BIS, 2015](#)). MOSWOC is mandated to produce daily space weather forecasts and is therefore developing a forecasting infrastructure using ground-based and satellite instrumentation to monitor space weather events. In addition, scientific research at MOSWOC

is carried out to better understand the physical processes involved in space weather phenomena to improve forecasting accuracy and lead-times; current forecasting enables prediction of CMEs impacting Earth to within only plus or minus six hours at best ([MetOffice, 2013](#)).

Forecasting and prediction is one aspect of the response to severe space weather events. We must also learn from the global response to the COVID-19 pandemic and ensure that upon the occurrence of a severe space weather event, suitable pre-planning has been performed and a sufficient contingent action is planned.

## 1.3 Cosmic Rays

### 1.3.1 Background

Cosmic Rays (CRs) are charged particles and atomic nuclei with energies spanning from 1 keV up to around  $10^{21}$  eV, that encroach upon the Earth from all directions ([Giacalone, 2010](#)). It is understood that CRs are composed of  $\sim 99\%$  of atomic nuclei and  $\sim 1\%$  electrons ([Gaisser et al., 2016](#)); of the atomic nuclei  $\sim 87\%$  are protons,  $\sim 12\%$  are  $\alpha$ -particles, and a smaller contribution of  $\sim 1\%$  are heavier nuclei of around  $\sim 1\%$  ([Grupen, 2005](#); [Dunai, 2010](#); [Particle Data Group et al., 2020](#)). CRs mainly originate from outside the solar system, known as Galactic Cosmic Rays (GCRs) ([Particle Data Group et al., 2020](#)). These GCRs mostly come from within the Milky Way, although they are also expected to emanate from extragalactic sources, in particular for CRs with energies above  $10^{18}$  eV ([Aab et al., 2017](#)). Incoming low-energy CRs ( $\lesssim 1$  GeV/nucleon) are modulated by the solar wind, which decelerates GCRs and can even forbid lower-energy GCRs from the inner solar system ([Grupen, 2005](#)). Consequently, there exists a strong anti-correlation between solar activity and the GCRs flux ([Particle Data Group et al., 2020](#)).

Cosmic rays produced within the heliosphere are mostly of solar origin, known as Solar Cosmic Rays (SCRs) or Solar Energetic Particles (SEPs). These SCRs are generally of a lower energy than GCRs and may be accelerated in the solar

wind, by interplanetary shocks, or in solar eruptions (e.g. solar flares) (Giacalone, 2010). SCRs have typical energies on the order of magnitude of  $\sim 10^1$  keV–1 GeV (Chilingarian, 2003; Bruno et al., 2018). Therefore, Primary Cosmic Rays (PCRs) associated with space weather events are generally of much lower energy than the background of GCRs.

The intensity spectrum of PCRs in the energy range from  $10^9$  eV to  $\sim 10^{14}$  eV is given approximately by:

$$I_N(E) = \frac{dN}{dE} \approx 1.8 \times 10^4 (E/1 \text{ GeV})^{-\alpha} \frac{\text{nucleons}}{\text{m}^2 \text{ sr GeV}}, \quad (1.2)$$

where  $E$  is the energy per nucleon (including rest mass energy) in GeV and  $\alpha = 2.7$  is the differential spectral index of the cosmic-ray flux (Particle Data Group et al., 2020).

Figure 1.6 shows a graphical representation of the CR energy spectrum described by equation (1.2). It shows the flux for a number of CR species, over the energy range  $10^{-1}$ – $10^6$  GeV/nucleus, measured by several different experiments.

Beyond the x-axis range in Figure 1.6, the spectrum ‘knee’ occurs (i.e. in the range  $\sim 10^{15}$ – $10^{16}$  eV) where the spectral index is thought to increase to  $\sim 3$  (Particle Data Group et al., 2020). At even higher energies, in the region of the spectrum ‘ankle’ ( $\sim 10^{18.5}$  eV) the spectral index reduces and the spectrum becomes less steep. This is in the regime of Ultra-High-Energy Cosmic Rays (UHECRs) and the interaction between GCRs and photons of the Cosmic Microwave Background (CMB) sets an upper limit on their energy, the Greisen-Zatsepin-Kuzmin (GZK) limit (Particle Data Group et al., 2020). The GZK limit implies that CRs with energies exceeding  $\sim 5 \times 10^{19}$  eV must have originated from distances within a horizon of  $\sim 50$  Mpc, as otherwise their energy would have been reduced by the GZK effect (Particle Data Group et al., 2020).

Propagation of CRs through magnetic fields depends on their gyroradius or Larmor radius (Particle Data Group et al., 2020). Therefore a common description of

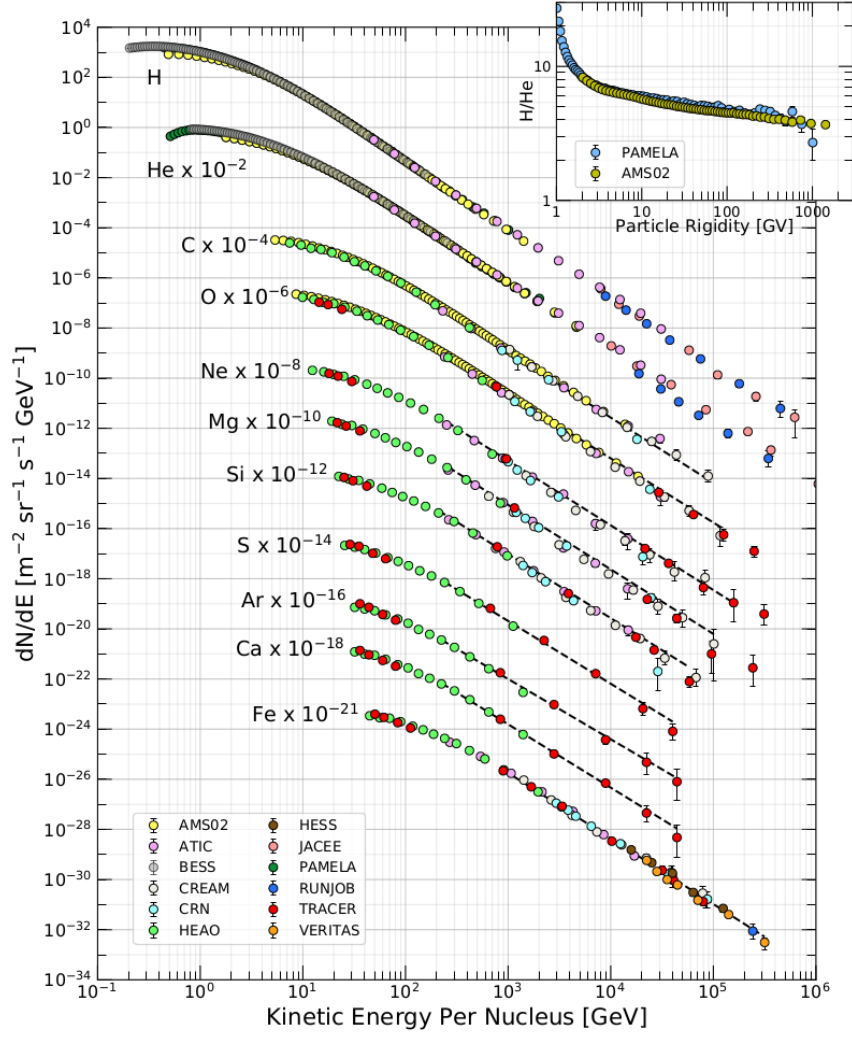


Figure 1.6: Cosmic ray differential energy spectrum using data measured by several experiments. The inset shows the H/He ratio at constant rigidity ([Particle Data Group et al., 2020](#))

CRs uses a property called the *magnetic rigidity* which is defined by:

$$R = r_L B c = \frac{p c}{Z e} \quad (1.3)$$

where  $r_L$  is the Larmor radius,  $B$  is the magnetic field strength,  $c$  is the speed of light,  $p$  is the particle's momentum,  $Z$  is the atomic number, and  $e$  is the electron charge. The magnetic rigidity has units of Volts (V), or usually due to a large magnitude, Gigavolts (GV). The rigidity is used to describe CRs as particles with different charges and masses have the same dynamics in a magnetic field if they have



the same rigidity ([Particle Data Group et al., 2020](#)).

### 1.3.2 Cosmic Rays in the Atmosphere

CRs in the interstellar medium traverse a very low-density medium, but experience a much denser environment when they reach the atmosphere. The typical nucleon mean free path (measured in units of  $\text{g cm}^{-2}$ ) of protons in the atmosphere is approximately  $90 \text{ g cm}^{-2}$ , which means the first interactions of CRs occur in the upper layers of the atmosphere, at a height of  $\sim 15\text{--}20 \text{ km}$  ([Grupen, 2005](#)).

The PCRs will predominantly interact with the atmospheric nuclei via strong interactions ([Grupen, 2005](#)). When PCRs interact with atmospheric nuclei, the interaction leads to the production of a cascade of secondary particles. The secondary particles can also undergo interaction or decay, producing tertiary particles, and the process continues until the energies of all particles are insufficient to create new particles. If a concentrated, large number of secondary particles reach ground-level, the cascade of particles is called an Air Shower (AS), or an Extensive Air Shower (EAS) for extremely high numbers of secondary particles, which can have a footprint area of several  $\text{km}^2$  [Fokkema \(2012\)](#); [van Dam et al. \(2020b\)](#)]. The AS is often described as being a cone, with the base being the shower front and the apex being the primary CR.

Hadronic cascade components (or the “hard component” of ASs) are produced by CR protons and nuclei interacting with atmospheric nuclei. This process typically produces lower energy protons, neutrons, pions, and kaons. In this thesis we are mostly interested in the muonic air shower development (see Section 1.4), so here we will focus on the development of the mesons in the ASs, as they predominantly produce muons. In Table 1.1, the most likely modes of decay for air shower mesons are shown with the branching ratio for each mode. In addition, the table shows the most likely decay modes of muons.

Due to the short lifetimes of pions and kaons,  $\sim 26 \text{ ns}$  and  $\sim 12 \text{ ns}$ , respectively

Table 1.1: Most prominent decay modes of the mesonic components of CR air showers and of muons. Note:  $K^-$  modes are charge conjugates of the decay modes below ([Particle Data Group et al., 2020](#))

Decay mode	Branching ratio
$\pi^+ \rightarrow \mu^+ + \nu_\mu$	$99.98770 \pm 0.00004\%$
$\pi^- \rightarrow \mu^- + \bar{\nu}_\mu$	$99.98770 \pm 0.00004\%$
$\pi^0 \rightarrow \gamma + \gamma$	$98.823 \pm 0.034\%$
$\pi^0 \rightarrow e^+ + e^- + \gamma$	$1.174 \pm 0.035\%$
$K^+ \rightarrow \mu^+ + \nu_\mu$	$63.56 \pm 0.11\%$
$K^+ \rightarrow \pi^+ + \pi^0$	$20.67 \pm 0.08\%$
$K^+ \rightarrow \pi^+ + \pi^+ + \pi^-$	$5.583 \pm 0.024\%$
$K^+ \rightarrow \pi^0 + e^+ + \nu_e$	$5.07 \pm 0.04\%$
$K^+ \rightarrow \pi^0 + \mu^+ + \nu_\mu$	$3.352 \pm 0.033\%$
$K^+ \rightarrow \pi^+ + \pi^0 + \pi^0$	$1.760 \pm 0.023\%$
$\mu^+ \rightarrow e^+ + \nu_e + \bar{\nu}_\mu$	$\sim 100\%$
$\mu^- \rightarrow e^- + \bar{\nu}_e + \nu_\mu$	$\sim 100\%$

([Particle Data Group et al., 2020](#)), and depending on energy, they decay during their journey to ground-level. It is shown in Table 1.1 that the most probable decay modes involve the production of muons. Muons are the most abundant charged particles at ground level ([Particle Data Group et al., 2020](#)). Most muons are produced high in the atmosphere ( $\sim 15$  km) and lose about 2 GeV to ionization before reaching the ground and the mean energy of muons at the ground is  $\sim 4$  GeV ([Particle Data Group et al., 2020](#)).

In addition to the hadronic component of an air shower, electron and photon constituents of cascades are called the electromagnetic component (or “soft component”). These are typically initiated by electrons and photons under the processes of Bremsstrahlung ([Gruppen, 2005](#)),

$$e \rightarrow e + \gamma, \quad (1.4)$$



or pair production ([Gruppen, 2005](#)),

$$\gamma \rightarrow e^- + e^+. \quad (1.5)$$

Ionisation losses mean that electrons and positrons lose energy rapidly until they either annihilate or recombine with nuclei, and photons lose their energy by being either absorbed in scattering and/or the photoelectric effect. Therefore most of the electrons, positrons, and photons observed at ground level are produced from the decaying hadronic AS component and muon decay is the dominant source of low-energy electrons at ground level ([Particle Data Group et al., 2020](#)).

Finally, there is a minimum rigidity cut-off which implies that the energy of any PCR must exceed a minimum energy to be able to initiate an AS or particle cascade and be measured at ground-level. This limit is dependent on the depth of the atmosphere above the detector, but is greatest at sea-level and decreases with increasing altitude. The minimum energy to be measured at sea-level is approx. 430 MeV/nucleon ([Dorman, 2004a,b](#); [Poluianov et al., 2017](#)).

### 1.3.3 Cosmic Ray Detectors

To observe CRs there are many types of usable detectors, both ground-based and space-based ([Schrijver & Siscoe, 2010](#)); in this thesis we are mostly concerned with ground-based detectors of the AS hadronic component. The most common type of ground-based CR detectors are Neutron Monitors (NMs) and Muon Detectors (MDs) which indirectly measure CR particles through the secondary particles produced in CR cascades. These two types of detector probe different energy ranges; NMs generally observe PCRs with energies  $\sim 1\text{--}10$  GeV and above, while MDs typically observe higher energy PCRs with energies on the order of  $\gtrsim 10$  GeV ([Kuwabara et al., 2006a](#); [Rockenbach et al., 2014](#)).

## Neutron Monitors

The neutron monitor, invented by [Simpson \(1948\)](#), has been extensively used for CR observations of the space environment ([Clem & Dorman, 2000](#)). The NM is an example of an ionisation detector whereby energetic neutrons encounter a nucleus within a gas, producing charged, secondary particles which in turn ionise the surrounding gas ([Gloeckler, 2010](#)).

The original “IGY” NM design made use of a paraffin reflector to trap slow neutrons within the detector, a producer material (typically lead) which multiplied the number of slow neutrons registered by the detector in order to amplify the signal, a moderator to further slow neutrons, and cylindrical proportional counters utilising  $\text{BF}_3$  gas ([Simpson, 1948](#); [Simpson et al., 1953](#)). A schematic diagram of the detector is shown in Figure 1.7a.

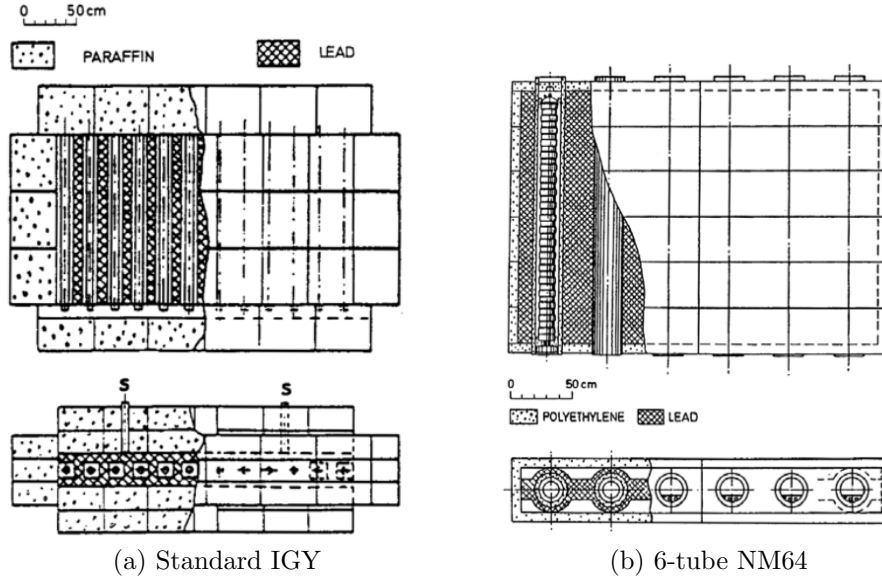


Figure 1.7: Schematic diagrams of two NM configurations: (a) the original Simpson’s 12-tube IGY NM is shown where the paraffin reflector is represented by the outer dotted blocks; the lead producer is represented by the cross-hatched section; the paraffin moderator is represented by the inner dotted blocks; finally the gas-filled proportional counters are denoted by the black circles/tubes. (b) the modern NM64 is shown on the right in its 6-tube configuration where the polyethylene reflector is represented by the outer dotted section; the lead producer is represented by the cross-hatched area; within the producer is a cylindrical polyethylene moderator denoted by the dotted ring; finally in the centre of each tube is a gas-filled proportional counter. In each figure the top schematic is a top-down drawing and the bottom is an end-on drawing. Taken from [Kang et al. \(2012\)](#).

An improved “NM64” NM design is now the preferred detector type, which makes use of a polyethylene reflector, lead producer, polyethylene moderator, and  $^{10}\text{BF}_3$  or  $^3\text{He}$  gas-filled cylindrical proportional counters (Kang et al., 2012). A schematic diagram of the detector is shown in Figure 1.7b. The new design provided an improvement over the IGY design by a factor of about 3.3 in the count rate per unit area of producer (Stoker et al., 2000); the choice of  $^{10}\text{BF}_3$  gas or  $^3\text{He}$  gas does not significantly affect the detector performance (Kang et al., 2012).

## Muon Detectors

Muon detectors are an example of a scintillation detector, whereby light emitted by atoms excited in a medium is collected and converted into an electrical signal. The scintillation medium can be solid, liquid, or gas; however solid scintillation detectors are attractive as they have a higher electron density (Gloeckler, 2010).

The general configuration of a MD is shown in Figure 1.8. When an energetic particle passes through a scintillator material, some of the particle’s energy is lost in ionising the scintillator material and the scintillator material releases photons. The light pipe directs the photons towards a Photo Multiplier Tube (PMT) where a cascade of electrons are produced and the resulting electrical signal is amplified and recorded through the back-end electronics.

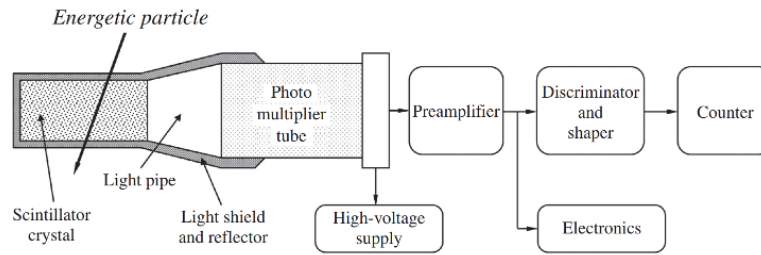


Figure 1.8: Schematic design of a typical scintillation muon detector with back-end electronics (Gloeckler, 2010)

Desirable properties of scintillator materials are a high conversion efficiency, transparency to the light that they emit, short fluorescent decay times, and spectral distributions suitable for photosensitive devices (Gloeckler, 2010).

A range of different material types are used in scintillator detectors however the most common scintillator materials for MDs are organic scintillators consisting of aromatic hydrocarbons (the fluors) in a solid plastic solvent (the base) (Gloeckler, 2010; Fokkema, 2012). Energetic particles traversing the scintillator excite the base rather than the fluor due to the low fluor density. The plastic base however has a low yield and is not transparent to its own scintillation light; thus the fluor is added to therefore increase the yield of this popular type of scintillator (Fokkema, 2012).

### 1.3.4 Cosmic Ray Observations of Solar Activity and Space Weather

It has long been established that there exists an anti-correlation between GCR intensity and the level of solar activity, over the  $\sim 11$ -year period (Forbush, 1958; Parker, 1965; Usoskin et al., 1998; Van Allen, 2000). We also see the 22-year Hale cycle manifesting in the GCR intensity, as interchanging peaked and flat-topped cycles of GCR intensity due to combination of solar activity and CR transport processes (Aslam & Badruddin, 2012; Thomas et al., 2014), as seen in Figure 1.9. The effects of solar activity on CRs observations are discussed in more details in the introduction to Chapter ??, since the analysis and interpretation of GCR data is presented in detail in that chapter.

There have been many documented observations of space weather events using CR detectors. The most notable types of CR space weather effects are Forbush Decreases (FDs) and Ground Level Enhancements (GLEs); here we discuss the properties of each.

#### Forbush Decreases

Short-term decreases in the GCR flux were first observed by Forbush (1937) and therefore were later coined as FDs or Forbush Effects (FEs). FDs are characterised by a sharp decrease in GCR intensity over a period of several hours–days, followed by a gradual recovery taking place over several days–a week (Cane, 2000; Belov,

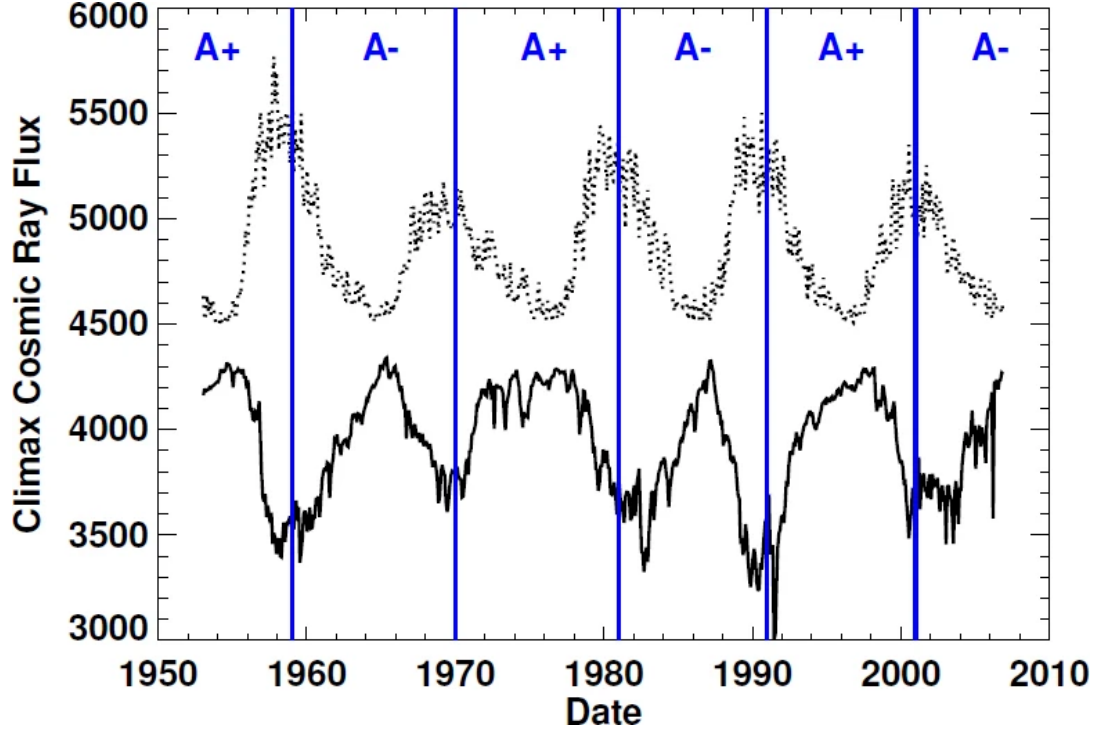


Figure 1.9: Cosmic ray flux measured at the Climax NM (solid line) and rescaled SSN (dotted line) taken from [Hathaway \(2015\)](#). The vertical lines denote changes in the Sun’s global magnetic field polarity, where: A+ indicates positive polarity at the North Pole; A– indicates negative polarity at the North Pole.

2008; [Wawrzynczak & Alania, 2010](#)), as shown in Figure 1.10.

There are two FD origins: one caused by Corotating Interaction Regions (CIRs) ([Dumbović et al., 2016](#)), and one caused by Interplanetary Coronal Mass Ejections (ICMEs) and the shocks they drive ([Belov, 2008](#)). The biggest FDs (magnitudes  $> 5\%$ ) are strictly associated with ICMEs ([Belov et al., 2001](#)). Of the kind caused by ICMEs, the majority are produced by ICMEs with speeds in the range 400–1200 km s<sup>−1</sup> ([Lingri et al., 2016](#)); the typical speed of the solar wind is, for slow solar wind, in the range 300–400 km s<sup>−1</sup>, and for fast solar wind,  $\sim 750$  km s<sup>−1</sup> ([Owens & Forsyth, 2013](#)). Previous literature has also shown that the type caused by CIRs produce recurrent, more symmetric, and lower-amplitude decreases ([Dumbović et al., 2012](#)), while the type caused by ICMEs result in the more strongly asymmetric decreases as shown in Figure 1.10 ([Lockwood, 1971](#); [Cane, 2000](#); [Dumbović et al., 2012](#)). In addition the ICME-driven FDs typically result in a two-step FD, where

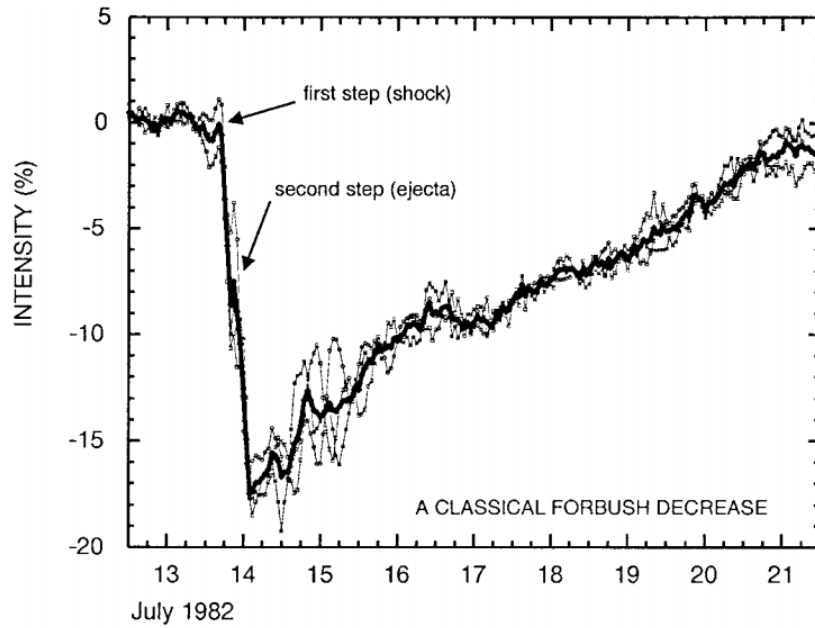


Figure 1.10: A two-step Forbush decrease measured at three NM stations, Deep River, Mt. Wellington, Kerguelen, in July 1982 (Cane, 2000). The thicker black line indicates the average of the count rates from the three stations. Arrows show the start of the two decreases caused by the shock and the ICME ejecta.

the first step of the decrease is due to the passage of the leading shock and the second step is due to the ICME itself, as shown in Figure 1.11 (Cane, 2000).

Lockwood (1971) showed that there is a rigidity dependence on the amplitudes of FDs, which is approximately related to  $R^{-\gamma}$ , where the exponent ranges from  $0.4 \lesssim \gamma \lesssim 1.2$ . In addition, Belov et al. (2001, 2014) showed the magnitude of the FD is proportional to the speed, mass, and width of the Coronal Mass Ejection (CME).

The Forbush Effects and Interplanetary-disturbances Database (FEID)<sup>2</sup> is a record of all the FDs observed since the beginning of the Global Neutron Monitor Network (GNMN) (Belov, 2008). The total number of events is  $\sim 7630$  during the epoch 1957–2020. Many studies have analysed observations of FDs using these data and investigated their features, driving factors, and precursors; for an overview see: Belov et al. (2001); Usoskin et al. (2008); Wawrzynczak & Alania (2010); Rockenbach et al. (2014); Arunbabu et al. (2015).

<sup>2</sup><http://spaceweather.izmiran.ru/eng/dbs.html>

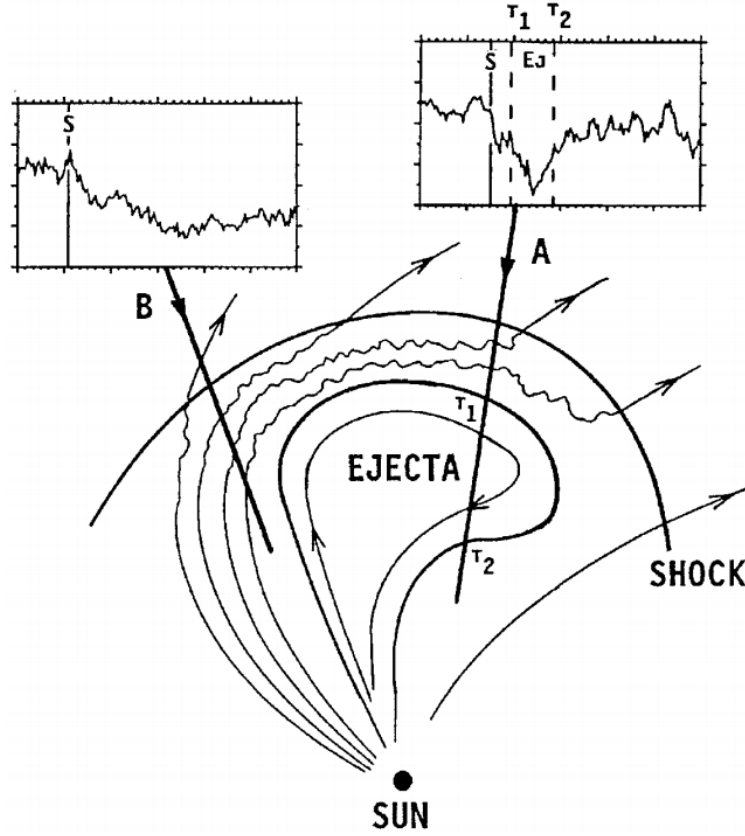


Figure 1.11: A schematic diagram of an ICME-driven FD taken from [Cane \(2000\)](#). It shows the different cosmic ray responses from two paths, indicated by A and B. A experiences the shock and ejecta, therefore experiencing a two-step FD; B only experiences the shock, therefore experiencing a single decrease. The time of shock passage is indicated by a solid, vertical line marked, S; the start and end times of ejecta passage are indicated by vertical, dashed lines marked T1 and T2, respectively.

## Ground Level Enhancements

Short-term increases in the GCR flux were first observed in the 1940s and early 1950s, but it was not until after the largest recorded event, in September 1956, that these increases were defined as GLEs ([Cramp, 1996](#)). GLEs are the detection of an increased number of the highest-energy portion ( $> 500$  MeV, [Kuwabara et al., 2006b](#)) of SEPs arriving at Earth along lines of Interplanetary Magnetic Field (IMF) following a solar eruptive event ([McCracken et al., 2012](#); [Poluianov & Usoskin, 2017](#)). The SEPs, which cause GLEs, can cause serious damage to satellite electronics and are a hazard to air crew and astronauts; hence, the monitoring of these events are of importance for space weather forecasting. GLEs are characterised by a sharp rise

in CR intensity over a period of several minutes–hours, followed by a gradual decay taking place over several hours, as shown in Figure 1.12.

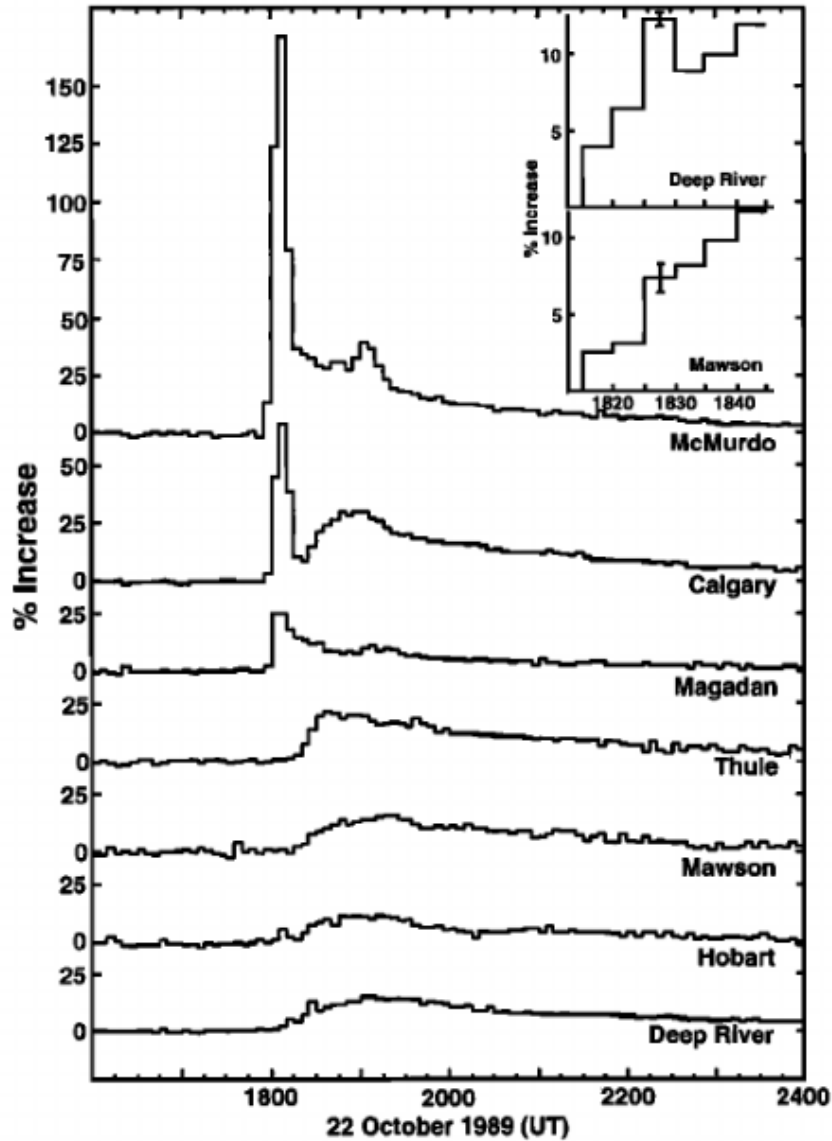


Figure 1.12: A GLE measured at nine NM stations in October 1989, taken from [Cramp, J. L. et al. \(1997\)](#).

GLEs result from energetic solar eruptions such as flares and CMEs ([McCracken et al., 2012](#)). The total number of GLEs observed to-date is low: there have been only 72. The GLE database<sup>3</sup> is a record of events, starting from GLE 5 (February 1956), since the beginning of the GNMN ([Usoskin et al., 2016](#)). Many studies have

<sup>3</sup><https://gle.oulu.fi>



discussed the observations of GLEs, investigating their features as well as the spectra and anisotropy of PCRs that produce the GLEs; for an overview see: [Shea & Smart \(1982\)](#); [Cramp \(1996\)](#); [Belov et al. \(2010\)](#); [McCracken et al. \(2012\)](#); [Strauss et al. \(2017\)](#); [Mishev et al. \(2018\)](#). [Strauss et al. \(2017\)](#) analysed the shapes of fourteen GLEs and showed the existence of a linear dependence between the rise and decay times which they empirically determined to be  $\tau_d \approx 3.5\tau_r$ .

The solar magnetic field is ‘frozen’ into the solar wind plasma. As the Sun rotates, so do the IMF lines which forms an Archimedean spiral, the Parker spiral ([Parker, 1958](#); [Parker & Jokipii, 1976](#)). A curved field line connecting the Sun to the Earth stems from the western limb of the Sun, at a longitude of about  $60^\circ$ , which is known as the ‘garden hose’ field line (see Fig. 1.13) ([Duldig et al., 1993](#); [Hathaway, 2015](#)). Charged particles follow magnetic field lines and therefore SEPs that are accelerated in flares located near to the solar end of the ‘garden hose’ field line usually arrive at Earth rapidly and have very sharp onsets ([Duldig et al., 1993](#); [Andriopoulou et al., 2011](#)). This causes a strong anisotropy in the arrival directions of the early SEPs inducing GLEs, as shown in Figure 1.12. The McMurdo, Calgary, and Magaden NM stations observed an earlier GLE onset, with a high magnitude, than the other stations ([Duldig et al., 1993](#); [Cramp, J. L. et al., 1997](#)). Conversely, GLEs associated with flares far from the ‘garden hose’ field line are usually delayed in their arrival at Earth, due to having to cross magnetic field lines, and have more gradual increases to maximum intensity ([Duldig et al., 1993](#)). Very few GLEs have originated far away from the base of the ‘garden hose’ at the solar surface ([Duldig et al., 1993](#); [Andriopoulou et al., 2011](#)).

The accepted definition of a GLE since the 1970s has been ([Poluianov et al., 2017](#)):

*a GLE event is registered when there are near-time coincident and statistically significant enhancements of the count rates of at least two differently located NMs.*

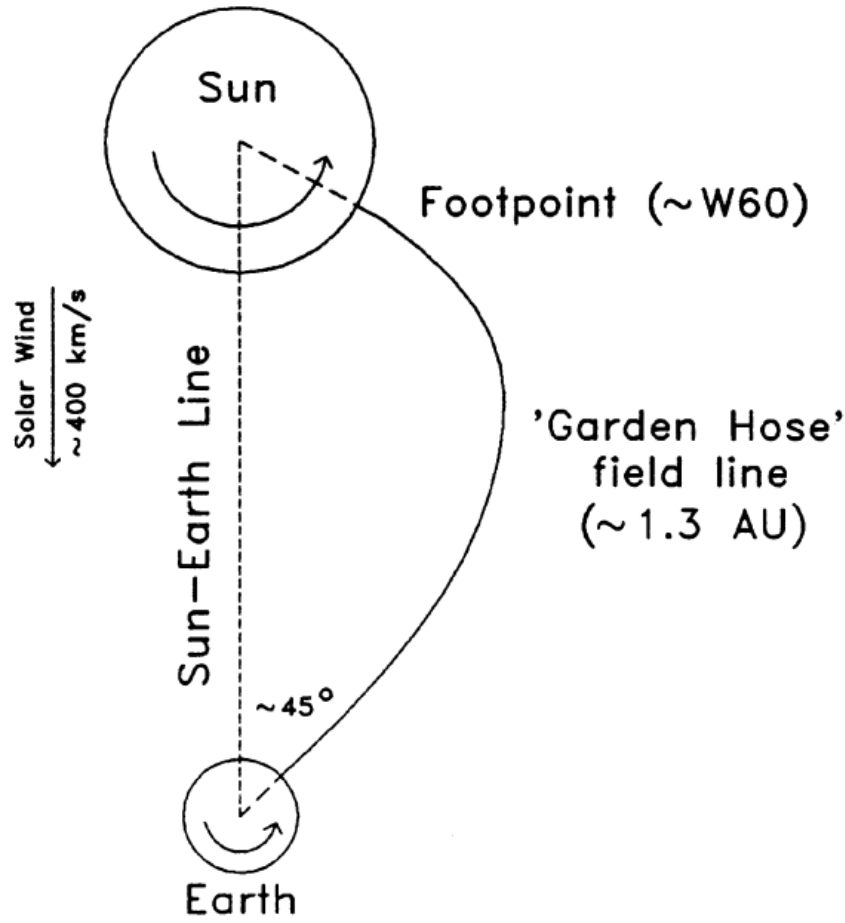


Figure 1.13: A schematic diagram of the ‘garden hose’ field line taken from [Duldig et al. \(1993\)](#).

However, recently a newer GLE definition has been adopted due to the increase in the number of NM stations that are more sensitive to lower energy CRs due to their high latitudes (i.e. in near-polar regions) or higher altitudes. It is a concern that these new NM stations will classify many more GLEs than their near-sea-level counterparts, thus affecting the homogeneity of the current list of GLEs ([Poluianov et al., 2017](#)). Therefore the new GLE definition is as follows ([Poluianov et al., 2017](#)):

*a GLE event is registered when there are near-time coincident and statistically significant enhancements of the count rates of at least two differently located neutron monitors, including at least one neutron monitor near sea-level and a corresponding enhancement in the proton flux measured by a space-borne instrument(s).*

The new definition also invoked the introduction of a sub-GLE class, defined as (Poluianov et al., 2017):

*a sub-GLE event is registered when there are near-time coincident and statistically significant enhancements of the count rates of at least two differently located high-elevation neutron monitors and a corresponding enhancement in the proton flux measured by a space-borne instrument(s), but no statistically significant enhancement in the count rates of neutron monitors near sea level.*

Finally, a GLE real-time alarm system was developed by Kuwabara et al. (2006a,b), using data from NMs and MDs, which has been shown to provide the earliest alert for the onset of SEP-driven space weather events. They showed their alerts provide a warning up to an hour earlier than the storm onset. Furthermore, they also show that through utilising the GNMN, monitoring precursory anisotropy, they can also issue warnings several hours ahead of near-Earth, in-situ satellite observations. They state that using both NMs and MDs provides a dual energy range for observations, providing a more effective system.

## 1.4 The HiSPARC Experiment

### 1.4.1 Background

The High School Project on Astrophysics and Research with Cosmics (HiSPARC) is a scientific outreach project that was initiated in the Netherlands in 2002 (Bartels, 2012). The HiSPARC experiment has two main goals: the study of Ultra-High-Energy Cosmic Ray (UHECR) for astroparticle physics research, and to serve as a resource to expose high school students to scientific research (Bartels, 2012).

HiSPARC is a global network of muon detectors spread across the Netherlands, Denmark, the UK, and Namibia. There are  $\sim 140$  stations in the HiSPARC network (van Dam et al., 2020b) which have been uploading data for varying durations since

2005. The detection philosophy of HiSPARC is to sample the footprints of Extensive Air Showers (EASs) using coincident triggers between scintillation detectors. The detectors at each station record muon counts and may be used for many scientific experiments, such as: reconstruction of the direction of a cosmic ray induced air shower, reconstruction of the energy of the air shower’s primary particle, investigation between the atmospheric conditions and the number of cosmic rays observed, etc. A comprehensive review of the HiSPARC experiment is provided by [Fokkema \(2012\)](#) and [van Dam et al. \(2020b\)](#).

The HiSPARC network has predominantly been used to study UHECRs, i.e. Primary Cosmic Rays (PCRs) with energies in excess of  $\sim 10^{14}$  eV. However, [van Dam et al. \(2020a\)](#) used the HiSPARC data to derive the Cosmic Ray (CR) flux at sea level for PCRs with energies between  $10^{12}$ – $10^{16}$  eV. Furthermore, [Fan & Velthuis \(2018\)](#) provided a study into the anti-correlation between atmospheric pressure and the HiSPARC data, as well as claiming to demonstrate the correlation between the daily-average of CR events and solar activity proxies.

### 1.4.2 HiSPARC Detector and Station Configuration

As HiSPARC was set up as an outreach programme for high schools, this impacted detector design [Fokkema \(2012\)](#); [van Dam et al. \(2020b\)](#). Resources are limited in schools and the detectors are usually financed by the participating high schools, colleges, and universities. In addition, students (accompanied by their teachers and local node support staff) are responsible for assembly and installation of their detectors, which are typically installed on the roofs of schools. Due to this, the detectors needed to be cheap, robust, and easily maintainable, therefore the scintillation detector was selected for the HiSPARC network.

Scintillators consist of materials that emit light when charged particles pass through them with sufficient energy to ionise the scintillator material. The total light produced is proportional to the number of charged particles, and can be col-

lected by a Photo Multiplier Tube (PMT). Each HiSPARC detector utilises a plastic scintillator of dimensions  $1000 \text{ mm} \times 500 \text{ mm} \times 20 \text{ mm}$ , providing a detection area of  $0.5 \text{ m}^2$ . A vertically incident Minimum Ionising Particle (MIP) has a most probable energy loss in 2 cm of the scintillation material of 3.51 MeV ( $\equiv 1 \text{ MIP}$ ) (van Dam et al., 2020b).

The scintillator is glued to a triangular/‘fish-tailed’ light-guide (dimensions, base: 500 mm; top: 25 mm; height: 675 mm), and a light-guide adapter provides the optical interface between the square end of the light-guide and the cylindrical aperture of the PMT. The configuration of a single HiSPARC detector is shown in Figure 1.14.

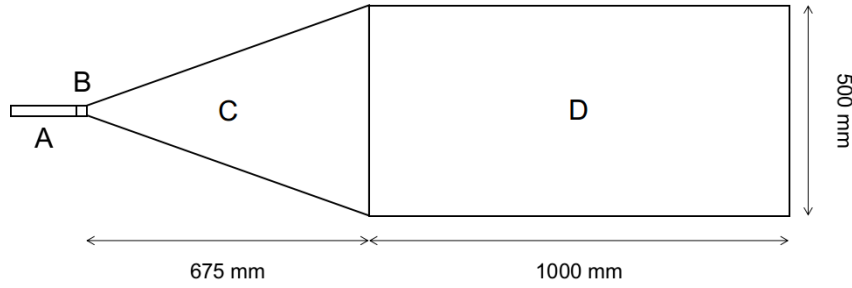


Figure 1.14: Schematic diagram of the HiSPARC scintillation detector. (A): PMT; (B): light-guide adapter; (C): light-guide; (D): scintillator.

The scintillator is made of a material consisting of polyvinyltoluene as the base, with anthracene as the fluor, and the emission spectrum peaks at a wavelength of 425 nm (Fokkema, 2012; Bartels, 2012). The light-guide is made from Polymethylmethacrylate (PMMA) and has a comparable refractive index to the scintillator (1.58 and 1.49, respectively), reducing refraction effects between the two materials (van Dam et al., 2020b).

The PMT used is an ETEnterprises 9125B model, with a 25 mm aperture, blue-green sensitive bialkali photocathode, and 11 high-gain dynodes (Bartels, 2012; ETEnterprises, 2020). The quantum efficiency of the PMT used in the HiSPARC detectors peaks at around 375 nm at 28%, and at 425 nm the quantum efficiency is 25% (Fokkema, 2012).

Each detector is wrapped in aluminium foil (thickness  $30 \text{ }\mu\text{m}$ ) and a black, vinyl

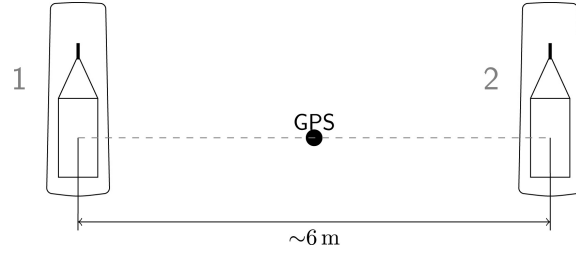
material (thickness 0.45 mm), which is usually used as a pond liner, to ensure light-tight detectors and to reduce the noise level from stray photons (van Dam et al., 2020b). In addition, each detector is placed inside its own a plastic roof box to again ensure that it is light-tight, and to also ensure that it is weather-proof, as the detectors are usually located on the roofs of schools, colleges, and universities.

The HiSPARC detectors have, individually, a high muon-detection efficiency close to 100% (Fokkema, 2012; van Dam et al., 2020b), therefore they are capable of observing any muons that traverse them. A HiSPARC station combines either 2 or 4 detectors, to observe coincident muons (‘events’), and typical configurations of each are shown in Figure 1.15. The separation between detectors varies from station-to-station and this influences the measurable footprint and hence the observable PCRs.

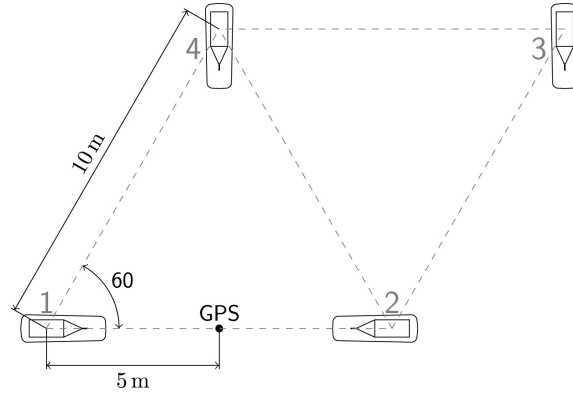
Furthermore some stations have the capability to measure the local atmospheric properties, such as temperature, pressure, relative humidity etc. Moreover, some stations also record the ‘singles’ rates, i.e. the frequency at which an individual detector is triggered, independently of the other detectors in the station. The singles rates are important when investigating non-EAS events.

The scientific goals that can be achieved also vary between the two- and four-detector stations. When at least three detectors in a four-detector station observe particles of an EAS, the direction of the EAS (and thus the direction of the PCR) can be acquired using triangulation calculations. When only two detectors in a station observe particles of an EAS it is only possible to reconstruct the arrival direction along the axis that connects the centres of those two detectors (thus it is not possible to reconstruct the direction of the PCR).

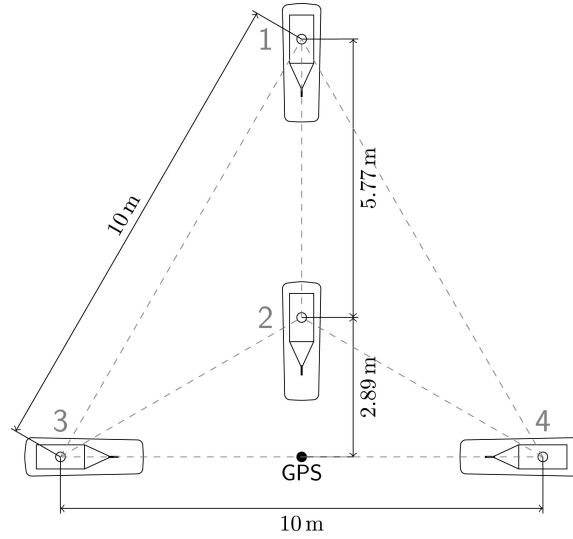
The PMTs of the detector in a station are connected to a HiSPARC electronics box, which samples and digitises the signal at a rate of 400 MHz, and each PMTs is connected to the electronics box using cables of a standard length of 30 m, to minimise any timing offsets between detectors (Fokkema, 2012; van Dam et al.,



(a) Two-detector station configuration



(b) Four-detector station configuration (triangle arrangement)



(c) Four-detector station configuration (diamond arrangement)

Figure 1.15: Typical formations of two-detector and four-detector stations ([Fokkema, 2012](#); [van Dam et al., 2020b](#)). In each, the black circle denotes a GPS antenna which is located in between the detectors to provide a precise timestamp for each signal.

2020b). A schematic diagram showing the configuration of, and interfaces between, the HiSPARC hardware is shown in Figure 1.16. The electronics boxes are capable of controlling and reading two PMTs (see Fig. 1.16), therefore a four-detector station requires two electronics boxes: a primary and a secondary.

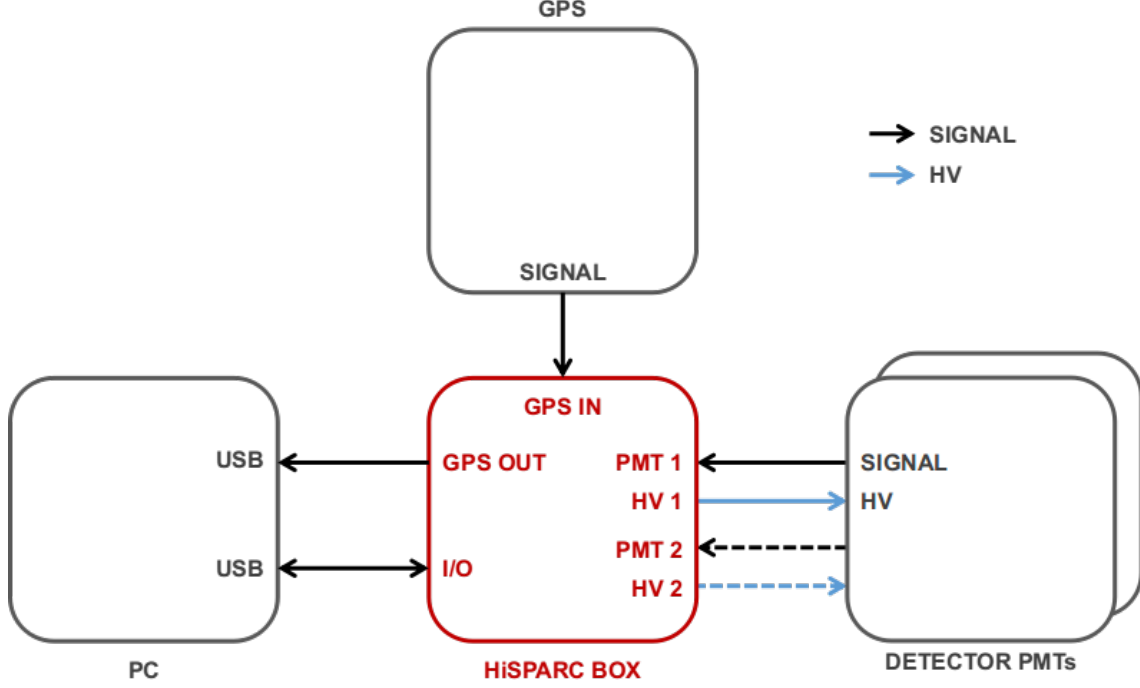


Figure 1.16: A schematic diagram showing the configuration and interfaces between the HiSPARC hardware for a two-detector station.

Figure 1.16 shows all the hardware interfaces with the HiSPARC electronics box, which communicates with the PC via USB. There are two connections for each PMT, one for the control (i.e. High Voltage (HV)) and another for the signal. In addition, a Global Positioning System (GPS) antenna is located in between the detectors in the station (shown in Fig. 1.15). The HiSPARC electronics box contains a GPS board, which provides an accurate timestamp for the data (Fokkema, 2012).

### 1.4.3 HiSPARC Data Acquisition

HiSPARC Data Acquisition (DAQ) software is used to control and read-out from the HiSPARC electronics box. The DAQ software was developed using LabVIEW, to be executed on a Windows PC (van Dam et al., 2020b). Figure 1.17a shows the



typical output signal from one of the PMTs, recorded by the DAQ software. The depth of the trace is called the *pulse height* and the area under the curve, the *pulse integral*. The pulse integral is a measure of the number of scintillation photons that have arrived at the PMT, exceeding the noise threshold ( $-10$  mV) (van Dam et al., 2020b). The HiSPARC DAQ software determines a signal baseline of the PMT (i.e. the background signal without an incident muon), the pulse height, and pulse integral.

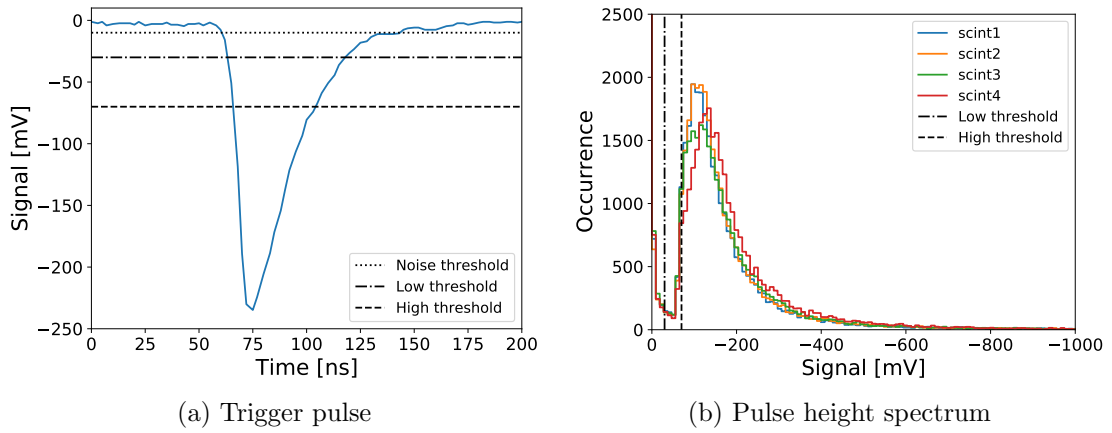


Figure 1.17: (a): An example PMT signal after digital conversion by the HiSPARC electronics box. The horizontal lines denote: the noise cut-off (dotted line), which is used for setting a limit when integrating the pulse height, to give the pulse integral; the low-voltage threshold (dash-dot); the high-voltage threshold (dashed). The role of the high- and low-voltage thresholds are described in the text below. (b) The pulse height distribution over the course of a single day from HiSPARC station 501. The vertical lines show the low-voltage threshold (dash-dot) and the high-voltage threshold (dashed).

The pulse height spectrum (see Fig. 1.17b) is a histogram of all the pulses recorded by a detector. It is composed of two main regions: the left side which falls off rather steeply, and the main, asymmetric part of the spectrum which features a peak and a long tail. The left side of the spectrum is understood to be from high-energy photons (gamma rays) produced in air showers (Fokkema, 2012). These high-energy photons may undergo pair production when interacting with the scintillator which may produce ionising electron and positron pairs.

The main, asymmetric distribution, which features a peak and a tail, is from charged particles (i.e. muons and electrons) (van Dam et al., 2020b). The mean

energy loss of particles in a material is described by the Bethe-Bloch formula; however, this does not account for fluctuations in energy loss and a Landau distribution describes the fluctuations in energy loss of particles (Fokkema, 2012). Due to the resolution of the HiSPARC detectors the distribution in Figure 1.17b is best described by the convolution of the Landau distribution and a normal distribution which describes the resolution of the detector (Fokkema, 2012). The peak of the distribution, the Most Probable Value (MPV), is the most likely energy lost by a particle in the detector, i.e. the 3.51 MeV (van Dam et al., 2020b). It has been shown that the location of the MPV can vary due to the effects of atmospheric temperature (Bartels, 2012; van Dam et al., 2020b).

For each PMT-channel, two discriminator thresholds can be defined: low- and high-voltage, as shown in Figure 1.17b, as vertical dash-dot and dashed lines, respectively. The trigger thresholds are placed to reject the noise signals from the data, i.e. the left side of the pulse height spectrum. If a signal exceeds the high threshold, there is a high probability that the signal was generated by a particle in the detector. The ‘singles’ data counts any time that the signal measured from a PMT exceeds the low- or high-threshold.

The HiSPARC experiment is configured in such a way as to ensure that each station across the HiSPARC network measures a similar count rate of muons, in order to aid the direct comparison between the different stations in the network. When configuring the station, a trigger threshold must be applied for the PMT signals. This is standardised across the HiSPARC network and can be seen in relation to a detector trigger pulse in Figure 1.17a. There are two thresholds, low:  $-30$  mV, which represents  $\sim 0.2$  of a MIP; high:  $-70$  mV, which represents  $\sim 0.5$  of a MIP (Fokkema, 2012; van Dam et al., 2020b). van Dam et al. (2020b) states the thresholds were chosen to increase the sensitivity for observing gamma rays and low-energy electrons; the sensitivity is lower than for muons. However, as the detectors can measure gamma rays and electrons, it can be difficult to determine whether

an individual detection was a muon, or another MIP, which is why the HiSPARC network usually relies on detecting ‘events’, from coincident muons.

To register an ‘event’, the detectors must measure signals which exceed the low threshold, within a limited time window. The time-line of the data acquisition during an event is given in Figure 1.18.

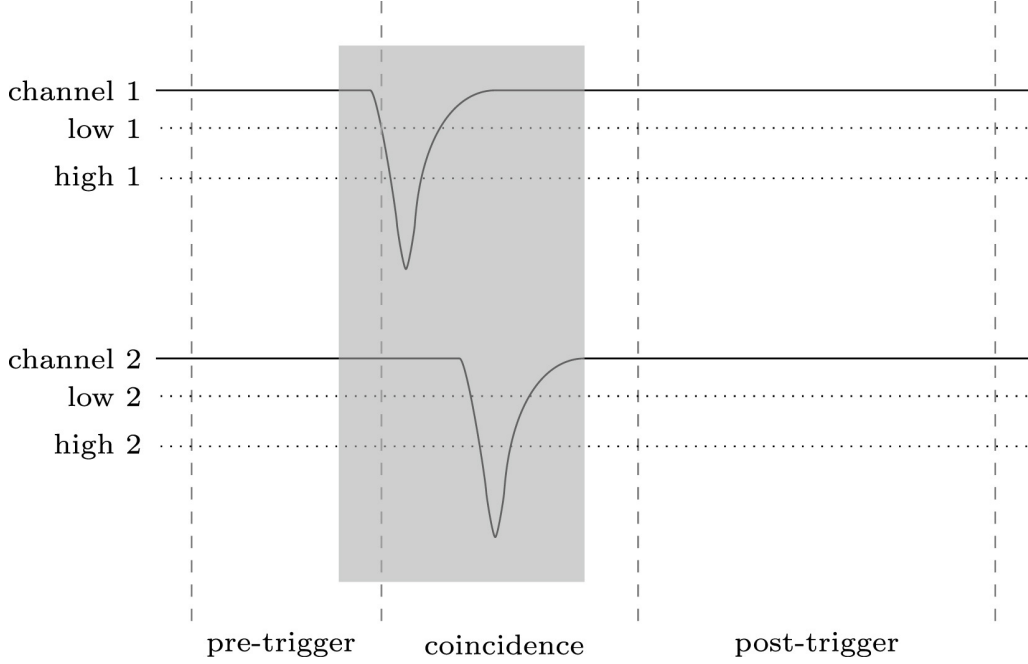


Figure 1.18: Schematic data acquisition of an event (Fokkema, 2012). The dashed vertical lines denote the epochs of the pre-trigger, coincidence, and post-trigger windows. The grey, shaded region shows the data reduction window and data outside this window are not stored. The dotted, horizontal lines denote the low- and high-voltage thresholds.

When channel 1 (i.e. PMT 1) exceeds the low-threshold a coincidence window is opened. The length of the coincidence window is  $\sim 1.5 \mu\text{s}$ . If, within this window, channel 2 (i.e. PMT 2) also measures a signal that exceeds the low threshold, the trigger condition is met and an event is generated. When a trigger is issued, the output is stored in the buffer of the Field Programmable Gate Array (FPGA) in the HiSPARC electronics box (Fokkema, 2012). The data acquisition software reads the data from the buffer and the full event data consist of: (i) data measured before the coincidence window was opened (the pre-trigger window, typical length  $\sim 1 \mu\text{s}$ ); (ii) data measured within the coincidence window; (iii) data measured after the trigger

period (the post-trigger window, typical length  $\sim 3.5 \mu\text{s}$ ). Therefore the event window lasts for  $\sim 6 \mu\text{s}$  in total, with the maximum length of an event window of  $10 \mu\text{s}$  (van Dam et al., 2020b). Finally, a data reduction algorithm is applied on the full event window which determines the part of the signal containing the muon pulses—compared to the baseline—and removes the rest, thus greatly reducing the size of the event data (Fokkema, 2012).

The default trigger condition for detecting an air shower event between multiple PMTs within a station differs for a two- and four-detector station. In a two-detector station, an event is recorded if the PMT signals from both detectors exceed the low threshold within the coincidence time window ( $1.5 \mu\text{s}$ ). In a four-detector station, the default trigger condition is either: (i) at least two detectors exceed the high threshold within the coincidence time window; (ii) at least three detectors exceed the low threshold within the coincidence time window. These are the default conditions, but there are other, user configurable ways of triggering the station.

Data recorded by the HiSPARC stations are stored and are available on the HiSPARC Public Database<sup>4</sup>, where each station is listed, grouped by local nodes. For every station one can see its ID, name, and a coloured square and circle displaying its current data delivery and DAQ status, respectively. Clicking on any station takes you to a dedicated page which displays its data on a user-selected day. Where data are available, it is possible to download:

- events rate data: where multiple detectors in a station are triggered to satisfy that station’s trigger condition;
- singles rate data: the count rates of the individual detectors within a station;
- weather data: meteorological data, including pressure and temperature;
- coincidences data: the counts where different stations measure the same event (to within  $1.36 \mu\text{s}$ ); it is possible to determine if stations measured the same

---

<sup>4</sup><https://data.hisparc.nl/>

event by comparing the GPS timestamps of events.

To support the HiSPARC project, the Simulation and Analysis Program Package for HiSPARC Research and Education (SAPPHiRE) Python package (Fokkema, 2012; Fokkema et al., 2012) was written. This Python package provide a framework to analyse the HiSPARC data, but also an alternative way to acquire the data.

## 1.5 Thesis Structure

In this thesis, a number of projects are presented which explore the themes of understanding the solar interior-atmosphere linkage and space weather applications. This is broken down into three major projects: a feasibility study on Cosmic Ray (CR) space weather applications, an investigation into the effects of solar activity on CR observations, and a study of the Solar Mean Magnetic Field (SMMF). The thesis is structured as follows:

In Chapter ?? we perform a feasibility study to determine whether the High School Project on Astrophysics and Research with Cosmics (HiSPARC) network is suitable for monitoring space weather events. This was achieved using historic data from the HiSPARC network to search for the signature of space weather events. In addition we performed simulations of Air Showers (ASs) to determine the expected variation in muon counts during space weather events. At the time of writing, the work in this chapter had not been published in any journals.

Following the results of Chapter ??, Chapter ?? outlines the design of an alternative HiSPARC station, with a novel arrangement of detectors that removes thermally induced, diurnal variations in the data, and reduces the existing energy bias of observable Primary Cosmic Rays (PCRs) using the HiSPARC network. In this chapter we discuss the set-up of the station, review the data and its noise properties, and finally also perform simulations using artificial data to investigate the capabilities of this new configuration. At the time of writing, the work in this chapter had not been published in any journals.

In Chapter ?? we studied long-term variations of Galactic Cosmic Ray (GCR) intensity in relation to the Sun Spot Number (SSN) during the most recent solar cycles. This study, which was published in the journal Solar Physics (Ross & Chaplin, 2019), analysed the time lag between the GCR intensity and the SSN, and the hysteresis effect of the GCR count rate against SSN for Solar Cycles 20–24.

Chapter ?? presents a frequency-domain analysis of over 20 years of high-cadence Birmingham Solar Oscillations Network (BiSON) observations of the SMMF. We modelled the power spectrum of the BiSON SMMF data to draw conclusions about the morphology of the SMMF, particularly focusing on the source of the rotationally modulated component in the signal. A significant portion of the work presented in this chapter was published in the journal Monthly Notices of the Royal Astronomical Society (Ross et al., 2021).

In Chapter ?? we further investigated the BiSON SMMF data. Here we examined the residual spectrum, after removing our best-fitting model, to search for evidence of a magnetic signature of global Rossby modes ( $r$  modes). At the time of writing, the work in this chapter had not been published in any journals.

Finally, the thesis is concluded in Chapter ??.

All of the work and results presented in this thesis are my own and all the data analysis was performed by me. Input from others came in the form of advice and consultation, in addition to the supply of raw data.

# Bibliography

- Aab A., et al., 2017, [Science](#), 357, 1266
- Andriopoulou M., Mavromichalaki H., Plainaki C., Belov A., Eroshenko E., 2011, [Sol Phys](#), 269, 155
- Arunbabu K. P., et al., 2015, [Astronomy and Astrophysics](#), 580, A41
- Aslam O. P. M., Badruddin 2012, [Solar Physics](#), 279, 269
- Augusto C., Navia C., de Oliveira M. N., Fauth A., Nepomuceno A., 2016, [Publ Astron Soc Jpn Nihon Tenmon Gakkai](#), 68
- BGS 2020, World Magnetic Model Calculator, [http://www.geomag.bgs.ac.uk/data\\_service/models\\_compass/wmm\\_calc.html](http://www.geomag.bgs.ac.uk/data_service/models_compass/wmm_calc.html)
- BIS 2015, Space weather preparedness strategy - GOV.UK. Vol. 2.1, <https://www.gov.uk/government/publications/space-weather-preparedness-strategy>
- Babcock H. W., 1953, [The Astrophysical Journal](#), 118, 387
- Babcock H. W., 1961, [The Astrophysical Journal](#), 133, 572
- Babcock H. W., Babcock H. D., 1955, [The Astrophysical Journal](#), 121, 349
- Bartels R. T., 2012, Technical report, The HiSPARC Experiment: An Analysis of the MPV and the Number of Events per Unit Time. University College Utrecht
- Basu S., Chaplin W. J., 2017, Asteroseismic Data Analysis: Foundations and Techniques
- Beggan C., Wild J., Gibbs M., 2018, [A&G](#), 59, 4.36
- Belov A. V., 2008, [Proceedings of the International Astronomical Union](#), 4, 439
- Belov A. V., Eroshenko E. A., Oleneva V. A., Struminsky A. B., Yanke V. G., 2001, [Advances in Space Research](#), 27, 625
- Belov A., Eroshenko E., Mavromichalaki H., Plainaki C., Yanke V., 2005, [Annales Geophysicae](#), 23, 2281
- Belov A. V., Eroshenko E. A., Kryakunova O. N., Kurt V. G., Yanke V. G., 2010, [Geomagn. Aeron.](#), 50, 21
- Belov A., et al., 2014, [Solar Physics](#), 289, 3949

- Berkova M. D., Belov A. V., Eroshenko E. A., Yanke V. G., 2011, [Bull. Russ. Acad. Sci. Phys.](#), 75, 820
- Blackmore E. W., Stukel M., Trinczek M., Slayman C., Wen S., Wong R., 2015, [IEEE Transactions on Nuclear Science](#), 62, 2792
- Braun I., Engler J., Hrandel J. R., Milke J., 2009, [Advances in Space Research](#), 43, 480
- Bruno A., et al., 2018, [The Astrophysical Journal](#), 862, 97
- CAEN 2011, User's Manual 00103/00:844-5.MUTx/07, Technical Information Manual: MOD. N844/N844P/N845 8-16 CHANNEL LOW THRESHOLD DISCRIMINATOR. CAEN
- Cabinet Office 2017, National Risk Register of Civil Emergencies - GOV.UK, 2017 edn. <https://www.gov.uk/government/publications/national-risk-register-of-civil-emergencies-2017-edition>
- Cane H. V., 2000, [Space Science Reviews](#), 93, 55
- Canfield R. C., 2001, in Murdin P., ed., , The Encyclopedia of Astronomy and Astrophysics. IOP Publishing Ltd, [doi:10.1888/0333750888/2023](https://doi.org/10.1888/0333750888/2023), <http://eaa.crcpress.com/0333750888/2023>
- Cannon P., Royal Academy of Engineering (Great Britain) 2013, Extreme space weather: impacts on engineered systems and infrastructure : summary report
- Carrington R. C., 1859, [Monthly Notices of the Royal Astronomical Society](#), 20, 13
- Carrington R. C., 1863, Observations of the spots on the sun from November 9, 1853, to March 24, 1861, made at Redhill. London [etc.] Williams and Norgate, <http://archive.org/details/observationsofsp00carr>
- Casanovas J., 1997, 118, 3
- Casas R., Vaquero J. M., Vazquez M., 2006, [Solar Physics](#), 234, 379
- Cecchini S., Sioli M., 2000, arXiv:hep-ex/0002052
- Chaplin W. J., et al., 2019, [Monthly Notices of the Royal Astronomical Society: Letters](#), 489, L86
- Chapman S. C., McIntosh S. W., Leamon R. J., Watkins N. W., 2020, [Geophysical Research Letters](#), 47, e2020GL087795
- Charbonneau P., 2020, [Living Reviews in Solar Physics](#), 17, 4
- Chilingarian A., 2003. CERN, Tsakhkadzor, Armenia, pp 63–79, <https://cds.cern.ch/record/604025/files/CERN-2005-007.pdf?page=73>
- Clark D. H., Stephenson F. R., 1978, Quarterly Journal of the Royal Astronomical Society, 19, 387
- Clem J. M., Dorman L. I., 2000, [Space Science Reviews](#), 93, 335



- Clette F., Lefvre L., 2016, *Solar Physics*, 291, 2629
- Clette F., Cliver E. W., Lefvre L., Svalgaard L., Vaquero J. M., Leibacher J. W., 2016, *Solar Physics*, 291, 2479
- Corti C., Potgieter M. S., Bindi V., Consolandi C., Light C., Palermo M., Popkow A., 2019, *ApJ*, 871, 253
- Covington A. E., 1969, *Journal of the Royal Astronomical Society of Canada*, 63, 125
- Cramp J. L., 1996, PhD Thesis, University of Tasmania, Hobart, <https://core.ac.uk/download/pdf/33327719.pdf>
- Cramp, J. L. Duldig, M. L. Flckiger, E. O. Humble, J. E. Shea, M. A. Smart, D. F. 1997, *Journal of Geophysical Research: Space Physics*, 102, 24237
- Danilova O. A., Demina I. M., Ptitsyna N. G., Tyasto M. I., 2019, *Geomagnetism and Aeronomy*, 59, 147
- Dasi-Espuig M., Solanki S. K., Krivova N. A., Cameron R., Peuela T., 2010, *Astronomy & Astrophysics*, 518, A7
- De Mendonça R. R. S., Raulin J. P., Echer E., Makhmutov V. S., Fernandez G., 2013, *J. Geophys. Res. Space Physics*, 118, 1403
- Desorgher L., 2005, Technical Report PLANETOCOSMICS-SUM, PLANETOCOSMICS Software User Manual, <http://cosray.unibe.ch/~laurent/planetocosmics/>. University of Bern
- Desorgher L., Flckiger E. O., Gurtner M., 2006. p. 2361, <http://adsabs.harvard.edu/abs/2006cosp...36.2361D>
- Dorman L. I., 1972, *Kosm. Luchi*, no. 13, pp. 5-66
- Dorman L. I., 2004a, in *Astrophysics and Space Science Library, Cosmic Rays in the Earths Atmosphere and Underground*. Springer, Dordrecht, pp 289–330, doi:10.1007/978-1-4020-2113-8\_5, [https://link.springer.com/chapter/10.1007/978-1-4020-2113-8\\_5](https://link.springer.com/chapter/10.1007/978-1-4020-2113-8_5)
- Dorman L. I., 2004b, in *Astrophysics and Space Science Library, Cosmic Rays in the Earths Atmosphere and Underground*. Springer, Dordrecht, pp 375–386, doi:10.1007/978-1-4020-2113-8\_7, [https://link.springer.com/chapter/10.1007/978-1-4020-2113-8\\_7](https://link.springer.com/chapter/10.1007/978-1-4020-2113-8_7)
- Dorman L. I., 2010, *Phys.-Usp.*, 53, 496
- Dubey A., Kumar S., Dubey S. K., 2016, *Journal of Physics: Conference Series*, 755, 012056
- Duldig M. L., et al., 1993, *Proceedings of the Astronomical Society of Australia*, 10, 211
- Dumbović M., Vršnak B., Čalogović J., Župan R., 2012, *Astronomy & Astrophysics*, 538, A28
- Dumbović M., Vršnak B., Čalogović J., 2016, *Sol Phys*, 291, 285

- Dunai T. J., 2010, in , *Cosmogenic Nuclides: Principles, Concepts and Applications in the Earth Surface Sciences*. Cambridge University Press, Cambridge, pp 1–24, [doi:10.1017/CBO9780511804519.003](https://doi.org/10.1017/CBO9780511804519.003)
- Dyer C. S., Lei F., Clucas S. N., Smart D. F., Shea M. A., 2003, *Advances in Space Research*, 32, 81
- ETEnterprises 2020, Technical Report 9125B, Data Sheet: 9125B Series, <http://et-enterprises.com/products/photomultipliers/product/p9125b-series>. ET Enterprises
- Fan K.-z., Velthuis J., 2018, arXiv:1808.10645 [astro-ph]
- Fesefeldt H., 1985, Technical Report PTHA-85/02, GHEISHA. The Simulation of Hadronic Showers: Physics and Applications. RWTH Aachen
- Fokkema D. B. R. A., 2012, PhD thesis, University of Twente
- Fokkema D. B. R. A., 2019, HiSPARC station software en hardware documentatie HiSPARC software 6.11 documentation, <https://docs.hisparc.nl/station-software/doc/index.html>
- Fokkema D. B. R. A., de Laat A. P. L. S., Kooij T., 2012, SAPPHERE, <https://github.com/HiSPARC/sapphire>
- Forbush S. E., 1937, *Physical Review*, 51, 1108
- Forbush S. E., 1958, *Journal of Geophysical Research*, 63, 651
- Gaisser T. K., Engel R., Resconi E., 2016, *Cosmic Rays and Particle Physics*, 2nd edn. Cambridge University Press, [doi:10.1017/CBO9781139192194](https://doi.org/10.1017/CBO9781139192194)
- Garca R. A., et al., 1999, *Astronomy and Astrophysics*, 346, 626
- Giacalone J., 2010, in Schrijver C. J., Siscoe G. L., eds, , *Heliophysics: Space Storms and Radiation: Causes and Effects*. Cambridge University Press, Cambridge, pp 233–262, [doi:10.1017/CBO9781139194532.010](https://doi.org/10.1017/CBO9781139194532.010)
- Gloeckler G., 2010, in Schrijver C. J., Siscoe G. L., eds, , *Heliophysics: Space Storms and Radiation: Causes and Effects*. Cambridge University Press, Cambridge, pp 233–262, [doi:10.1017/CBO9781139194532.004](https://doi.org/10.1017/CBO9781139194532.004)
- Gnevyshev M. N., 1938, *Pulkovo Obs. Circ*, 24, 37
- Gnevyshev M. N., 1963, *Soviet Astronomy*, 7, 311
- Gnevyshev M. N., 1967, *Solar Physics*, 1, 107
- Gopalswamy N., 2010, pp 108–130
- Gopalswamy N., Yashiro S., Michalek G., Stenborg G., Vourlidas A., Freeland S., Howard R., 2009, *Earth, Moon, and Planets*, 104, 295

- Government H., 2020, Risk Register, National Risk Register: 2020 edition, [https://assets.publishing.service.gov.uk/government/uploads/system/uploads/attachment\\_data/file/952959/6.6920\\_CO\\_CCS\\_s\\_National\\_Risk\\_Register\\_2020\\_11-1-21-FINAL.pdf](https://assets.publishing.service.gov.uk/government/uploads/system/uploads/attachment_data/file/952959/6.6920_CO_CCS_s_National_Risk_Register_2020_11-1-21-FINAL.pdf). HM Government
- Groom D. E., Mokhov N. V., Striganov S. I., 2001, *Atomic Data and Nuclear Data Tables*, 78, 183
- Gruppen C., 2005, *Astroparticle Physics*. Springer-Verlag, Berlin Heidelberg, doi:10.1007/3-540-27670-X, <https://www.springer.com/gp/book/9783540253129>
- Hagenaar H. J., 2001, *ApJ*, 555, 448
- Hale G. E., Nicholson S. B., 1925, *The Astrophysical Journal*, 62, 270
- Hale G. E., Ellerman F., Nicholson S. B., Joy A. H., 1919, *The Astrophysical Journal*, 49, 153
- Harvey K., 2001, in , *The Encyclopedia of Astronomy and Astrophysics*. IOP Publishing Ltd, doi:10.1888/0333750888/2275, <http://eaa.crcpress.com/0333750888/2275>
- Harvey K. L., Martin S. F., 1973, *Solar Physics*, 32, 389
- Harvey K. L., Zwaan C., 1993, *Solar Physics*, 148, 85
- Hathaway D. H., 2015, *Living Rev. Sol. Phys.*, 12, 4
- Hathaway D. H., Upton L. A., 2017, *Solar Cycle Science*, <http://solarcyclescience.com/index.html>
- Heck D., Pierog T., 2017, Technical Report 7.6400, Extensive Air Shower Simulation with CORSIKA: A Users Guide
- Herbst K., Kopp A., Heber B., 2013, *Annales Geophysicae*, 31, 1637
- Homeier N., Wei L., 2013, Technical report, Solar Storm Risk to the North American Electric Grid, <https://www.lloyds.com/news-and-risk-insight/risk-reports/library/natural-environment/solar-storm>. Lloyd's
- Howard R. F., 2001, in , *The Encyclopedia of Astronomy and Astrophysics*. IOP Publishing Ltd, doi:10.1888/0333750888/2297, <http://eaa.crcpress.com/0333750888/2297>
- Humble J. E., Duldig M. L., Smart D. F., Shea M. A., 2012, *Geophysical Research Letters*, 18, 737
- Kang J., Jang D. Y., Kim Y., Kang B. H., Kim Y.-K., Kim J., Park H., Yi Y., 2012, *Journal of the Korean Physical Society*, 61, 720
- Keller C. U., Schssler M., Vögler A., Zakharov V., 2004, *ApJ*, 607, L59
- Kiepenheuer K. O., ed. 1968, *Structure and Development of Solar Active Regions*. International Astronomical Union Symposia, Springer Netherlands, doi:10.1007/978-94-011-6815-1, <https://www.springer.com/gp/book/9789027701220>
- Knipp D. J., et al., 2016, *Space Weather*, 14, 2016SW001423

- Kudela K., Storini M., Hofer M. Y., Belov A., 2000, [Space Science Reviews](#), 93, 153
- Kuwabara T., et al., 2006a, [Space Weather](#), 4, S08001
- Kuwabara T., Bieber J. W., Clem J., Evenson P., Pyle R., 2006b, [Space Weather](#), 4, S10001
- LISIRD 2019, Solar Radio Flux at 10.7cm, Time Series, [https://lasp.colorado.edu/lisird/data/penticton\\_radio\\_flux/](https://lasp.colorado.edu/lisird/data/penticton_radio_flux/)
- LeCroy 1996, LeCroy Research Systems Model 365AL, Model 465, and Technical Data: Model 622 Logic Units, <https://teledynelecroy.com/lrs/dsheets/365al.htm>
- Leamon R. J., McIntosh S. W., Marsh D. R., 2018, arXiv e-prints, 1812, arXiv:1812.02692
- Leamon R. J., McIntosh S. W., Chapman S. C., Watkins N. W., 2020, [Solar Physics](#), 295, 36
- Lee 1858, [Monthly Notices of the Royal Astronomical Society](#), 19, 1
- Lei F., Clucas S., Dyer C., Truscott P., 2004, [IEEE Transactions on Nuclear Science](#), 51, 3442
- Leighton R. B., 1964, [The Astrophysical Journal](#), 140, 1547
- Lingri D., Mavromichalaki H., Belov A., Eroshenko E., Yanke V., Abunin A., Abunina M., 2016, arXiv:1612.08900 [astro-ph]
- Lista L., 2016, Statistical Methods for Data Analysis in Particle Physics. Lecture Notes in Physics, Springer International Publishing, doi:10.1007/978-3-319-20176-4, <https://www.springer.com/gp/book/9783319201764>
- Lockwood J. A., 1971, [Space Science Reviews](#), 12, 658
- Lockwood M., Stamper R., Wild M. N., 1999, [Nature](#), 399, 437
- Luminet J.-P., 2017, arXiv:1701.02930 [physics]
- Martin S. F., 1988, [Solar Physics](#), 117, 243
- Martin S. F., Harvey K. L., 1979, [Solar Physics](#), 64, 93
- Maunder E. W., 1903, *The Observatory*, 26, 329
- Maunder E. W., 1904, [Mon Not R Astron Soc](#), 64, 747
- McCracken K. G., Moraal H., Shea M. A., 2012, [ApJ](#), 761, 101
- McIntosh S. W., et al., 2014, [ApJ](#), 792, 12
- McIntosh S. W., Leamon R. J., Egeland R., Dikpati M., Fan Y., Rempel M., 2019, [Sol Phys](#), 294, 88
- McIntosh S. W., Chapman S., Leamon R. J., Egeland R., Watkins N. W., 2020, [Solar Physics](#), 295, 163

- Mendonça R. R. S. d., et al., 2016, *ApJ*, 830, 88
- MetOffice 2013, Technical Report 13/0402, Space Weather, [https://www.metoffice.gov.uk/binaries/content/assets/mohippo/pdf/public-sector/emergencies/space-weather/space\\_weather\\_datasheet\\_final.pdf](https://www.metoffice.gov.uk/binaries/content/assets/mohippo/pdf/public-sector/emergencies/space-weather/space_weather_datasheet_final.pdf)
- Mishev A. L., Usoskin I. G., Raukunen O., Paassilta M., Valtonen E., Kocharov L. G., Vainio R., 2018, *Solar Physics*, 293
- Mishra R. K., Mishra R. A., 2007, *Pramana*, 68, 407
- Mishra R. K., Mishra R. A., 2008, *Rom. Journ. Phys.*, 53, 925
- Montanus H., 2017, PhD thesis, University of Amsterdam, [https://www.nikhef.nl/pub/services/biblio/theses\\_pdf/](https://www.nikhef.nl/pub/services/biblio/theses_pdf/)
- NMDB 2018, NMDB Event Search Tool (NEST), <http://www.nmdb.eu/nest/>
- NOAA 2018, NOAA Space Weather Predictions Center, <https://www.swpc.noaa.gov/>
- Nature 1871, Observations Upon Magnetic Storms in Higher Latitudes, [doi:10.1038/004441a0](https://www.nature.com/articles/004441a0), <https://www.nature.com/articles/004441a0>
- Nelson W. R., Hirayama H., Rogers D. W. O., 1985, Technical Report SLAC-265, EGS4 code system, <https://www.osti.gov/biblio/6137659-egs4-code-system>. Stanford Linear Accelerator Center, Menlo Park, CA (USA)
- Norton A. A., Gallagher J. C., 2009, *Solar Physics*, 261, 193
- Ostapchenko S., 2006, *Nuclear Physics B - Proceedings Supplements*, 151, 143
- Owens M. J., Forsyth R. J., 2013, *Living Rev. Sol. Phys.*, 10, 5
- Parker E. N., 1958, *The Astrophysical Journal*, 128, 664
- Parker E. N., 1965, *Planetary and Space Science*, 13, 9
- Parker G. D., Jokipii J. R., 1976, *Geophysical Research Letters*, 3, 561
- Particle Data Group et al., 2020, *Progress of Theoretical and Experimental Physics*, 2020
- Paschalis P., Mavromichalaki H., Yanke V., Belov A., Eroshenko E., Gerontidou M., Koutroumpi I., 2013, *New Astronomy*, 19, 10
- Pereira E. G., Vasconcellos C. A. Z., Hadjimichef D., 2020, arXiv:2011.06480 [hep-ex, physics:hep-ph]
- Pesnell W. D., 2020, *Journal of Space Weather and Space Climate*, 10, 60
- Pillet V. M., Lites B. W., Skumanich A., 1997, *ApJ*, 474, 810
- Poluianov S., Usoskin I. G., 2017, in Proceedings of Science. Bexco, Busan, Korea, <https://pos.sissa.it/301/#session-3145>
- Poluianov S. V., Usoskin I. G., Mishev A. L., Shea M. A., Smart D. F., 2017, *Sol Phys*, 292, 176

- Riley P., 2012, [Space Weather](#), 10
- Rockenbach M., et al., 2014, [Space Sci Rev](#), 182, 1
- Ross E., Chaplin W. J., 2019, [Sol Phys](#), 294, 8
- Ross E., Chaplin W. J., Hale S. J., Howe R., Elsworth Y. P., Davies G. R., Nielsen M. B., 2021, [Monthly Notices of the Royal Astronomical Society](#)
- Russell C. T., et al., 2013, [ApJ](#), 770, 38
- SILSO WDC 2020, International Sunspot Number Monthly Bulletin and online catalogue
- Salvatier J., Wiecki T. V., Fonnesbeck C., 2016, [PeerJ Comput. Sci.](#), 2, e55
- Sanchez S., Fournier A., Pinheiro K. J., Aubert J., Sanchez S., Fournier A., Pinheiro K. J., Aubert J., 2014, [Anais da Academia Brasileira de Cincias](#), 86, 11
- Savić M., Maletić D., Joković D., Veselinović N., Banjanac R., Udovičić V., Dragić A., 2015, [J. Phys.: Conf. Ser.](#), 632, 012059
- Scherrer P. H., Wilcox J. M., Kotov V., Severnyj A. B., Severny A. B., Howard R., 1977a, [Solar Physics](#), 52, 3
- Scherrer P. H., Wilcox J. M., Svalgaard L., Duvall Jr. T. L., Dittmer P. H., Gustafson E. K., 1977b, [Solar Physics](#), 54, 353
- Schrijver C. J., Harvey K. L., 1994, [Solar Physics](#), 150, 1
- Schrijver C. J., Siscoe G. L., eds, 2010, [Heliophysics: Space Storms and Radiation: Causes and Effects](#). Cambridge University Press, Cambridge, doi:10.1017/CBO9781139194532, <https://www.cambridge.org/core/books/heliophysics-space-storms-and-radiation-causes-and-effects/608857F4EEE1COBF61F26ACD19BA59DE>
- Schrijver C. J., Zwaan C., 2008, [Solar and Stellar Magnetic Activity](#). Cambridge University Press
- Schwabe H., 1844, [Astronomische Nachrichten](#), 21, 233
- Schwenn R., 2006, [Living Reviews in Solar Physics](#), 3, 2
- Shea M. A., Smart D. F., 1982, [Space Science Reviews](#), 32, 251
- Shea M. A., Smart D. F., McCracken K. G., 1965, [J. Geophys. Res.](#), 70, 4117
- Sheeley N. R., 2005, [Living Reviews in Solar Physics](#), 2, 5
- Simpson J. A., 1948, [Phys. Rev.](#), 73, 1389
- Simpson J. A., Fonger W., Treiman S. B., 1953, [Phys. Rev.](#), 90, 934
- Solanki S. K., 2003, [The Astronomy and Astrophysics Review](#), 11, 153
- Solanki S. K., Schssler M., Fligge M., 2000, [Nature](#), 408, 445

- Solanki S. K., Schssler M., Fligge M., 2002, [A&A](#), 383, 706
- Solovov A. A., Parfinenko L. D., Efremov V. I., Kirichek E. A., Korolkova O. A., 2019, [Astrophysics and Space Science](#), 364, 222
- Spruit H. C., 1976, [Solar Physics](#), 50, 269
- Stoker P. H., Dorman L. I., Clem J. M., 2000, [Space Science Reviews](#), 93, 361
- Strauss R. D., Ogunjobi O., Moraal H., McCracken K. G., Caballero-Lopez R. A., 2017, [Solar Physics](#), 292, 51
- Svalgaard L., Wilcox J. M., Scherrer P. H., Howard R., 1975, [Sol Phys](#), 45, 83
- Tapping K. F., 2013, [Space Weather](#), 11, 394
- Tapping K. F., Charrois D. P., 1994, [Solar Physics](#), 150, 305
- Tapping K. F., DeTracey B., 1990, [Solar Physics](#), 127, 321
- Thébault E., et al., 2015, [Earth, Planets and Space](#), 67, 79
- Thomas S. R., Owens M. J., Lockwood M., 2014, [Sol Phys](#), 289, 407
- Thomas S., Owens M., Lockwood M., Owen C., 2017, [Ann. Geophys.](#), 35, 825
- Timashkov D. A., et al., 2008, [Astroparticle Physics](#), 30, 117
- Tsyganenko N. A., 1989, [Planetary and Space Science](#), 37, 5
- Tsyganenko N. A., 2013, [Annales Geophysicae](#), 31, 1745
- Usoskin I. G., Kananen H., Mursula K., Tanskanen P., Kovaltsov G. A., 1998, [Journal of Geophysical Research: Space Physics](#), 103, 9567
- Usoskin I. G., Braun I., Gladysheva O. G., Hörandel J. R., Jmsn T., Kovaltsov G. A., Starodubtsev S. A., 2008, [J. Geophys. Res.](#), 113, A07102
- Usoskin I., Ibragimov A., Shea M. A., Smart D., 2016, in Proceedings of The 34th International Cosmic Ray Conference PoS(ICRC2015). Sissa Medialab, The Hague, The Netherlands, p. 054, [doi:10.22323/1.236.0054](#), [https://pos.sissa.it/236/054](#)
- Van Allen J. A., 2000, [Geophysical Research Letters](#), 27, 2453
- Vieira L. E. A., Solanki S. K., 2010, [A&A](#), 509, A100
- Viljanen A., 2011, [Space Weather](#), 9, 07007
- Waldmeier M., 1955, [Quarterly Journal of the Royal Meteorological Society](#), 82, 118
- Wawrzynczak A., Alania M. V., 2010, [Advances in Space Research](#), 45, 622
- Webb D. F., Howard R. A., 1994, [Journal of Geophysical Research: Space Physics](#), 99, 4201
- Wolf R., 1856, *Astronomische Mittheilungen der Eidgenössischen Sternwarte Zurich*, 1, 3

- Wolf R., 1859, [Monthly Notices of the Royal Astronomical Society](#), 19, 85
- Wolf R., 1861, [Monthly Notices of the Royal Astronomical Society](#), 21, 77
- Yashiro S., Gopalswamy N., Michalek G., Cyr O. C. S., Plunkett S. P., Rich N. B., Howard R. A., 2004, [Journal of Geophysical Research: Space Physics](#), 109
- Zwaan C., 1981, NASA Special Publication, 450
- eFoam 2017, SF38 High Foam Datasheet, <https://www.efoam.co.uk/docs/SF38.pdf>
- van Dam K., van Eijk B., Steijger J. J. M., 2020a, arXiv:2009.05308 [astro-ph]
- van Dam K., van Eijk B., Fokkema D. B. R. A., van Holten J. W., de Laat A. P. L. S., Schultheiss N. G., Steijger J. J. M., Verkooijen J. C., 2020b, [Nuclear Instruments and Methods in Physics Research Section A: Accelerators, Spectrometers, Detectors and Associated Equipment](#), 959, 163577
- van Driel-Gesztelyi L., Green L. M., 2015, [Living Rev. Sol. Phys.](#), 12, 1